Rotation curve fitting and its fatal attraction to cores in realistically simulated galaxy observations

Juan C. B. Pineda,[1]★ Christopher C. Hayward,[2,3,4] Volker Springel[5,6] and Claudia Mendes de Oliveira[1]

[1]*Instituto de Astronomia, Geofísica e Ciências Atmosféricas, Universidade de São Paulo, R. do Matão 1226, 05508-090 São Paulo, Brazil*
[2]*Center for Computational Astrophysics, Flatiron Institute, 162 Fifth Avenue, New York, NY 10010, USA*
[3]*TAPIR 350-17, California Institute of Technology, 1200 E. California Boulevard, Pasadena, CA 91125, USA*
[4]*Harvard–Smithsonian Center for Astrophysics, 60 Garden Street, Cambridge, MA 02138, USA*
[5]*Heidelberger Institut für Theoretische Studien, Schloss–Wolfsbrunnenweg 35, D-69118 Heidelberg, Germany*
[6]*Zentrum für Astronomie der Universität Heidelberg, Astronomisches Recheninstitut, Mönchhofstr. 12-14, D-69120 Heidelberg, Germany*

ABSTRACT

We study the role of systematic effects in observational studies of the cusp–core problem under the minimum disc approximation using a suite of high-resolution (25-pc softening length) hydrodynamical simulations of dwarf galaxies. We mimic realistic kinematic observations and fit the mock rotation curves with two analytic models commonly used to differentiate cores from cusps in the dark matter distribution. We find that the cored pseudo-isothermal sphere (ISO) model is strongly favoured by the reduced χ_ν^2 of the fits in spite of the fact that our simulations contain cuspy Navarro–Frenk–White profiles (NFW). We show that even idealized measurements of the gas circular motions can lead to the incorrect answer if velocity underestimates induced by pressure support, with a typical size of order ~ 5 km s^{-1} in the central kiloparsec, are neglected. Increasing the spatial resolution of the mock observations leads to more misleading results because the inner region, where the effect of pressure support is most significant, is better sampled. Fits to observations with a spatial resolution of 100 pc (2 arcsec at 10 Mpc) favour the ISO model in 78–90 per cent of the cases, while at 800-pc resolution, 41–77 per cent of the galaxies indicate the fictitious presence of a dark matter core. The coefficients of our best-fitting models agree well with those reported in observational studies; therefore, we conclude that NFW haloes cannot be ruled out reliably from this type of analysis.

Key words: galaxies: dwarf – galaxies: haloes – galaxies: kinematics and dynamics – galaxies: structure – cosmology: theory – dark matter.

1 INTRODUCTION

In the last decades, cosmological numerical simulations based on the Λ cold dark matter (ΛCDM) concordance model have substantially improved our understanding of the dynamical evolution of the Universe on large scales (Davis et al. 1985; Springel et al. 2005; Boylan-Kolchin et al. 2009; Angulo et al. 2012; Klypin et al. 2016). More recently, it has also become possible to include baryons in large cosmological volumes and directly follow galaxy formation, with very promising results (Vogelsberger et al. 2014a; Schaye et al. 2015). However, a number of well-documented small-scale discrepancies between ΛCDM and observations still remain to be

understood, including the so-called cusp–core problem concerning the inner structure of galactic dark matter (DM) haloes (Flores & Primack 1994; Moore 1994). On one hand, DM haloes assembled in cosmological simulations exhibit cuspy radial density profiles which steeply increase towards the centre (Navarro, Frenk & White 1996b, 1997; Moore et al. 1999; Klypin et al. 2001; Navarro et al. 2004; Diemand et al. 2005; Stadel et al. 2009). They are fairly well represented by the Navarro–Frenk–White (NFW) fitting formula (Navarro et al. 1996b), with an asymptotic behaviour of $\rho_{\rm inner} \propto r^{-1}$. On the other hand, kinematic observations of disc galaxies (via rotation curves) and dwarf spheroidals (via stellar velocity dispersions) often seem to be more compatible with core-like DM haloes ranging from $\rho_{\rm inner} \propto r^0$ to $\rho_{\rm inner} \propto r^{-0.3}$ (Flores & Primack 1994; de Blok et al. 2001; Salucci 2001; de Blok & Bosma 2002; Kuzio de Naray et al. 2006; Spano et al. 2008;

★ E-mail: basto-pineda@usp.br; juan.basto.pineda@gmail.com

Oh et al. 2011a, 2015; Walker & Peñarrubia 2011). A number of studies have also inferred intermediate slopes, which do not evidence constant-density cores but still are substantially shallower than canonical cusps from simulations (Simon et al. 2005; Adams et al. 2014).

Several physical mechanisms have been proposed to reconcile these findings and explain the origin of DM cores. The current leading picture invokes repetitive starburst episodes and the associated supernovae feedback to blow out central baryons and induce rapid changes in the gravitational potential (Navarro, Eke & Frenk 1996a; Gelato & Sommer-Larsen 1999; Read & Gilmore 2005; Mashchenko, Wadsley & Couchman 2008; Governato et al. 2010, 2012; Madau, Shen & Governato 2014; Pontzen & Governato 2014; Chan et al. 2015; Oñorbe et al. 2015). However, many feedback implementations do not form cores (Lia et al. 2000; Gnedin & Zhao 2002; Ceverino & Klypin 2009), which has not precluded the formation of realistic galaxies (Sawala et al. 2010; Marinacci, Pakmor & Springel 2014) as well as realistic populations of galaxies at $z = 0$ in fully cosmological runs (Vogelsberger et al. 2014c; Schaller et al. 2015). Also, there are lingering doubts (Garrison-Kimmel et al. 2013) regarding whether the available supernova energy is actually sufficient to create cores of the alleged size.

From the observational point of view, a problematic issue of using rotation curves to probe the DM density profiles is to accurately account for the stellar gravitational potential, mainly because of the uncertain mass-to-light conversion factor (van Albada et al. 1985; Bell & de Jong 2001; Bershady et al. 2010). One way around this problem lies in studying DM-dominated systems, such as late-type dwarf irregulars and low surface brightness (LSB) galaxies. For these systems, it is acceptable to use the minimum disc approximation, i.e. to ignore the existence of baryons and use the observed rotation curves at face value to derive an indicative upper limit on the amount of DM (de Blok & McGaugh 1997; de Blok et al. 2001; Spekkens, Giovanelli & Haynes 2005; Kuzio de Naray et al. 2006). Furthermore, different observations suggest that LSBs are characterized by a comparatively quiescent evolution, which likely implies relatively unperturbed DM haloes, making them very interesting for cosmology (de Blok, van der Hulst & Bothun 1995; Impey & Bothun 1997; Du et al. 2015). Indeed, these kinds of galaxies have been a main target of observational studies and represent some of the most acute challenges for the ΛCDM cosmogony, as their rotation curves are interpreted by several authors as strong evidence for DM cores (de Blok et al. 2001; de Blok & Bosma 2002; Simon et al. 2003; Oh et al. 2011a, 2015). However, some studies find some dwarfs and some LSB galaxies to be compatible with CDM cusps or claim that available data simply do not allow us to differentiate cusps from cores (e.g. van den Bosch et al. 2000; van den Bosch & Swaters 2001; Swaters et al. 2003; Simon et al. 2005; Spekkens et al. 2005; Valenzuela et al. 2007). The systematic uncertainties involved in studying this problem are a matter of active debate in the literature.

A number of effects that may lower the inner rotation curves and potentially mask cusps and make them appear as cores have been investigated over the years. For instance, early H I rotation curves had poor spatial resolution and were considerably affected by beam smearing. This motivated the gathering of high-resolution optical data for which beam smearing is expected to no longer be a problem (Blais-Ouellette et al. 1999; Swaters, Madore & Trewhella 2000), though it may still play a role in the very inner measurements, specially for distant galaxies (Swaters et al. 2003). More recently, some surveys of H I in very nearby galaxies, like THINGS (Walter

et al. 2008) and LITTLE THINGS (Hunter et al. 2012) [amongst others, e.g. Begum et al. (2008); Ott et al. (2012)], have also reached the necessary resolution to alleviate beam-smearing concerns. The first Hα rotation curves were obtained from long-slit spectroscopy, with the associated risk of missing the kinematic centre of the galaxy or its major axis; fortunately, this is no longer an issue since high-resolution velocity fields have become available (Blais-Ouellette, Amram & Carignan 2001; Garrido et al. 2002). Other problems that can be assessed by means of 2D velocity maps are possible offsets between the photometric and kinematic centres and the presence of non-circular motions (Simon et al. 2005; Oh et al. 2008). A detailed analysis of these effects for a sample of 19 galaxies from THINGS was presented by Trachternach et al. (2008), who concluded that these effects are rather small and the sample is hence suitable for the mass modelling studies presented in de Blok et al. (2008).

Projection effects related to the thickness of gaseous discs are also potentially problematic because mixing of material along the line of sight tends to lower the inferred circular velocity (Rhee et al. 2004). Additionally, pressure exerted by the gas can effectively lower the gravitational radial acceleration, thus lowering the rotational velocity needed for support. With very few exceptions (e.g. Oh et al. 2011a), pressure support corrections are usually neglected because they are expected to be small (de Blok & Bosma 2002). Halo triaxiality has also been considered as a possible explanation for the cusp–core discrepancy (Hayashi, Navarro & Springel 2007), but using both observations and numerical modelling, other authors have argued that this is not likely to be the case (Simon et al. 2005; Kuzio de Naray, McGaugh & Mihos 2009; Kazantzidis, Abadi & Navarro 2010; Kuzio de Naray & Kaufmann 2011). Besides all the potential complications already mentioned, we note that galaxies are often irregular and present substructures such as bars, bulges, and spiral arms. In addition, rotation curves are often wiggled, warped, or lopsided. The interpretation of these features and their impact on the cusp–core problem is not clear and cannot be modelled from first principles.

A powerful approach to study these systematic effects is by means of controlled experiments with simulated data. The first attempts in this direction mimicked long-slit observations of analytic velocity fields, including some uncertainties. In this way, de Blok, Bosma & McGaugh (2003) concluded that it should be possible to recognize the real steepness of a DM halo from its measured rotation curve and that no single systematic effect can account for the cusp–core difference. However, following the same approach, Swaters et al. (2003) concluded that systematic effects tend to erase the signature of cusp-like haloes and that rotation curve analyses cannot compellingly rule out the presence of cusps. Similarly, Spekkens et al. (2005) found cuspy DM haloes to be consistent with the observed distribution of slopes once systematic effects are taken into account. Dutton et al. (2005) pointed out that uncertainties inherent in mass modelling studies prevent them from setting firm constraints on the shape of DM haloes. Kuzio de Naray et al. (2009) did not use analytic velocity fields but instead integrated orbits numerically. They mimicked 2D integral field unit data using a reference sample of observations and concluded that if present at all, NFW haloes should be still recognizable. However, although these kinds of models provided useful insights into the problem, they were clearly oversimplifications. For instance, with the exception of Dutton et al. (2005), these studies assumed infinitely thin massless discs, and none included hydrodynamics.

Rhee et al. (2004) brought analyses of observations and simulations closer together. They performed *N*-body simulations of stellar discs inside cuspy haloes and *observed* them in a realistic

manner, concluding that projection effects, small bulges, and bars can often lead to false detections of DM cores. Valenzuela et al. (2007) confirmed these results using simulated analogues of the dwarf galaxies NGC 3109 and NGC 6822. They also compared a pure *N*-body simulation with hydrodynamical runs and suggested that pressure support related to stellar and supernova feedback can also produce the illusion of cores. A different result from similar simulations was presented by Kuzio de Naray & Kaufmann (2011). They concluded that the signatures of cores, cusps, and triaxiality in DM haloes should be clearly detectable in observed velocity fields. In recent work, Oh et al. (2011b) analysed mock observations of two dwarf galaxies formed in zoom-in cosmological simulations that undergo the supernovae-driven cusp-to-core transformation (Governato et al. 2010) and compared them with a sample of dwarfs from the THINGS survey. Oh et al. (2011b) found that their mock observations trace the true rotation curves and true surface density profiles of the simulated galaxies fairly well. They also state that their simulations are a good match to real galaxies regarding these quantities, but Oman et al. (2015) showed that the alleged agreement is only apparent in some cases. Moreover, Oman et al. (2015) demonstrated that the diversity of dwarf galaxy rotation curves is much greater than that of galaxies formed in cosmological simulations, posing a new challenge to any model trying to solve the cusp–core problem. Recently, Read et al. (2016) addressed this question using mock observations from a suit of very high-resolution (4 pc) simulations and indicate that at least part of the observed diversity can be explained from the starburst cycles of galaxies and their influence on the dynamical state of the galaxy.

Given the body of in part contradictory conclusions in the literature, it is apparent that further investigations of potential systematic effects in observational inferences about the cusp–core problem are worthwhile. In this work, we carry out a comprehensive theoretical study of the kinematics of a set of simulated dwarf galaxies by carefully creating synthetic observations that are then analysed in exactly the same manner as real data. In this way, we can determine the effects of different sources of error in the context of the cusp–core problem and assess to what extent these errors can lead to misleading inferences about the structure of the analysed galaxies. Here, we focus on the minimum disc approximation, exploiting the fact that our models are DM dominated at all radii, and we only use rotation curve fitting to classify cusps and cores; a complementary analysis using rotation curve inversion methods will be presented in a separate paper, as they demand a different approach.

The outline of the paper is as follows. In Section 2, we present our simulated galaxy sample and summarize the simulation methodology. In Section 3, we introduce the methods we use to analyse the information from the snapshots. In Section 4, we present the dynamical evolution of the different components, the mock observed rotation curves, and the results from the rotation curve fitting methods that aim to distinguish cusps from cores. In Section 5, we discuss the systematic effects that influence these results, aiming to disentangle the effects of spatial resolution, inclination, pressure support, etc. Finally, in Section 6 we present our conclusions and a summary of our results.

2 SIMULATIONS

2.1 Physical characteristics of the simulated galaxies

We simulate six dwarf galaxies in isolation at high resolution using the *N*-body+smoothed-particle hydrodynamics (SPH) code GADGET-2 (Springel 2005). Each simulation is composed of a DM halo plus an exponential disc of stars and gas, as summarized in Table 1. The methods for creating the numerical realizations of the initial conditions are essentially the same as described in Springel (2005) and Cox (2004). Here, we hence focus on the motivation for choosing the physical parameters of the galaxies and only briefly mention the most relevant technical details.

Galaxy models 'Dwarf1' to 'Dwarf4' (or simply D1,..., D4) are representative of the bulk of the properties of observed late-type dwarfs and LSBs (e.g. de Blok & Bosma 2002; Spekkens et al. 2005; de Blok et al. 2008; Kuzio de Naray, McGaugh & de Blok 2008; Kuzio de Naray et al. 2009; Stark, McGaugh & Swaters 2009; Oh et al. 2011a). These four galaxies are constructed to lie on the stellar and baryonic Tully–Fisher relations (TF) of Bell & de Jong (2001). Note that if both TF relations are required to be satisfied simultaneously, this puts a constraint on the gas fraction as a function of the stellar mass. Using representative values from Bell & de Jong (2001), we define the following target relations:

$$\log(M_\star) = 0.83 + 4.34 \log(v_{\text{flat}}), \tag{1}$$

$$f_{\text{g}} = \frac{M_{\text{gas}}}{M_{\text{gas}} + M_\star} = 1 - \frac{M_\star^{0.21}}{170}, \tag{2}$$

where $M_\star$ and M_{gas} are the total masses of the stellar and the gaseous discs, f_{g} is the gas fraction, and v_{flat} is the maximum circular velocity. The radial stellar and gaseous distributions drop exponentially, with surface density profiles given by

$$\Sigma_\star(r) = \frac{M_\star}{2\pi h_0^2} e^{-r/h_0}, \tag{3}$$

$$\Sigma_{\text{gas}}(r) = \frac{M_{\text{gas}}}{2\pi h_{\text{gas}}^2} e^{-r/h_{\text{gas}}}. \tag{4}$$

The stellar scalelengths are chosen to be relatively large (but still realistic) in order to give our galaxies a low surface brightness. We

Table 1. Properties of the six simulated galaxies.

Model	M_{halo}[a] ($M_\odot$)	N_{halo}[b] ($\times 10^6$)	c[c]	$M_\star$[d] ($M_\odot$)	$N_\star$[e] ($\times 10^6$)	h_0[f] (kpc)	z_0[g] (kpc)	M_{gas}[h] ($M_\odot$)	N_{gas}[i] ($\times 10^6$)	h_{gas}[j] (kpc)	f_{g}[k]	v_{flat}[l] (km s^{-1})
Dwarf1	3.0×10^{10}	1.5	11	1.2×10^8	0.1	0.8	0.16	3.7×10^8	0.3	2.4	0.76	57
Dwarf2	7.0×10^{10}	3.5	11	6.0×10^8	0.5	1.7	0.34	1.1×10^9	0.9	5.1	0.65	78
Dwarf3	1.2×10^{11}	6.0	10	1.2×10^9	1.0	2.5	0.5	1.6×10^9	1.4	7.8	0.57	89
Dwarf4	2.6×10^{11}	6.5	10	6.0×10^9	1.2	3.0	0.6	3.4×10^9	0.7	9.0	0.36	119
G0	5.1×10^{10}	1.3	14	1.0×10^9	0.2	1.1	0.22	6.1×10^8	0.1	3.3	0.38	67
G1	2.0×10^{11}	5.0	12	5.0×10^9	0.3	1.5	0.3	2.0×10^9	0.1	4.5	0.29	103

[a]Halo mass; [b]Number of particles in DM halo; [c]Halo concentration; [d]Stellar mass; [e]Number of stellar particles; [f]Stellar disc scalelength; [g]Stellar disc scaleheight; [h]Gas mass; [i]Number of gas particles; [j]Gaseous disc scalelength; [k]Gas fraction relative to baryonic mass; [l]Maximum rotation velocity.

make the gaseous discs three times more extended than the stellar ones as suggested by observations (Broeils & van Woerden 1994).

The vertical structure of the stellar discs follows a typical $\mathrm{sech}^2(z/z_0)$ model with the scaleheight z_0 equal to one-fifth of the radial scalelength h_0, so their 3D density fields read

$$\rho_\star(r, z) = \frac{M_\star}{4\pi h_0^2 z_0} e^{-r/h_0} \mathrm{sech}^2(z/z_0). \qquad (5)$$

For gaseous discs, the vertical structure is self-consistently calculated considering the full gravitational potential and assuming hydrodynamic equilibrium under a given equation of state that we choose to be the multiphase model of Springel & Hernquist (2003).

DM haloes are modelled with the cuspy NFW density profile (Navarro et al. 1996b). We did not simulate cored haloes because several mechanisms that might cause cusps to appear as cores have been proposed, but no mechanisms that can cause cores to appear as cusps are known. Moreover, to provide a potential solution to the cusp–core problem, it is only necessary to demonstrate that cusps can be mistaken for cores. The original NFW formulation is

$$\rho_{\mathrm{NFW}}(r) = \frac{\rho_o}{(r/R_s)[1 + (r/R_s)]^2}. \qquad (6)$$

In equation (6), ρ_o is a characteristic density and R_s represents a transition radius between an inner and an outer exponential law ($\rho_{\mathrm{inner}} \sim r^{-1}$; $\rho_{\mathrm{outer}} \sim r^{-3}$). An alternative parametrization that provides easier comprehension of the halo structure is obtained by casting the enclosed mass into a circular velocity profile,

$$v_{\mathrm{NFW}}(r) = v_{200}\sqrt{\frac{\log(1 + cx) - cx/(1 + cx)}{x[\log(1 + c) - c/(1 + c)]}}, \qquad (7)$$

with v_{200} representing the circular velocity at r_{200}, the radius at which the halo mean density is 200 times the critical density for closure.[1] The parameter $c \equiv r_{200}/R_s$ measures the central concentration of the mass distribution, and $x \equiv r/r_{200}$.

For each galaxy, the halo mass is chosen as a function of the stellar mass following the abundance matching relation of Guo et al. (2010). The concentrations are determined using the halo mass–concentration relation at redshift zero (Ludlow et al. 2014), which is a fundamental outcome of large cosmological simulations. Guo et al. (2010) used the Chabrier (2003) initial mass function (IMF), whereas Bell & de Jong (2001) used a scaled-down Salpeter (1955) IMF, giving rise to a systematic difference of 0.15 dex in stellar mass. For this reason, we add 0.15 dex to the actual stellar mass when we use equations (1) and (2) to define the target v_{flat} and f_g, respectively. Compared to the stellar masses at face value, this increment raises the target circular velocities by 8 per cent and the target gaseous masses by 10–25 per cent.

Once we have defined an initial configuration, we create the corresponding initial conditions file and check if v_{flat} actually satisfies the TF relations inside the expected scatter, slightly adjusting the halo parameters otherwise. As a side effect of this tuning, the less massive galaxies, D1 and D2, end up with DM haloes that are less massive than predictions from the abundance matching target relation. Nevertheless, through a comparison with different samples from the literature, Oh et al. (2011a) have noted that this is not at odds with observations of low-mass galaxies, for which the abundance matching relation of Guo et al. (2010) is not directly constrained but rather represents an extrapolation to smaller masses.

[1] Note that v_{200} encodes the halo mass through $M_{200} = v_{200}^3/(10GH_0)$; we use $H_0 = 70$ km s^{-1} Mpc^{-1}.
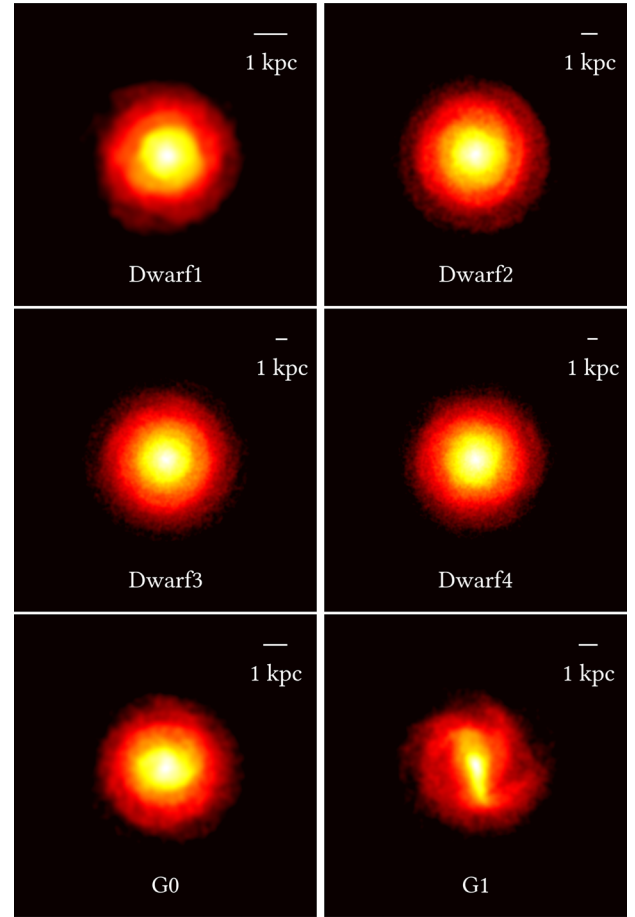
Figure 1. Face-on stellar density maps of our simulated galaxies at half the simulation time (3 Gyr). Note that with the exception of G1, the simulated galaxies do not exhibit non-axisymmetric structures such as spiral arms or bars.

We also checked that our galaxies are consistent with the baryonic TF relation of Stark et al. (2009), which was calibrated specifically using small, gas-rich galaxies (mainly dwarf galaxies and LSBs). Additionally, we require v_{flat} to stay below 130 km s^{-1}, following the selection criterion of Spekkens et al. (2005) to characterize a galaxy as a dwarf. We note that galaxy models D1 to D4 retain well-behaved discs throughout the simulation. There are neither detectable signatures of central bulge-like mass concentrations nor formation of bars, spiral arms, or other baryonic substructures (see Figs 1 and 2).

We also re-simulated two galaxies from the sample of Cox (2004). These models are, by construction, representative of late-type galaxies in the local Universe, as their main properties, such as disc size, dynamical mass, and gas fraction, are consistent with a large set of observations (Roberts & Haynes 1994). From the sample of Cox (2004), we only included the systems with $v_{\mathrm{flat}} < 130$ km s^{-1}, G0 and G1. The DM haloes exhibit NFW density profiles with numerical parameters tuned to match the baryonic TF relation from Bell & de Jong (2001). We note that these parameters are quite consistent with the scheme we propose for Dwarfs 1–4 regarding the stellar mass–halo mass and halo mass–concentration relations. G0's halo mass is lower than the abundance matching prediction, but it is consistent with observed galaxies of similar mass, as already discussed for D1 and D2. A major difference between our models and Cox (2004) is that we omitted the bulge component in the initial
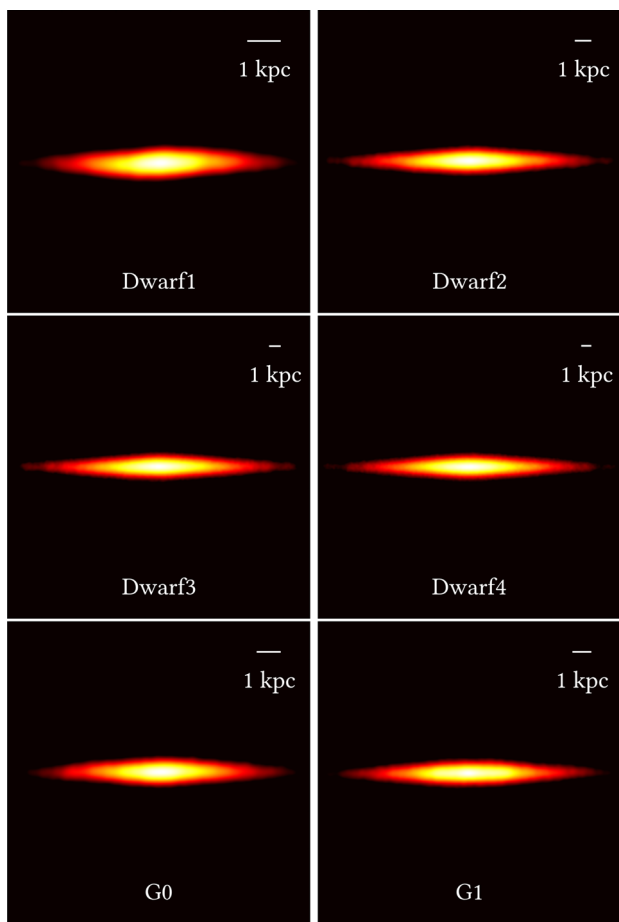
Figure 2. Edge-on stellar density maps after 3 Gyr of evolution. Our galaxies do not form bulge-like central concentrations of matter.

setup. To minimize perturbations in the original target relations, we redistribute the bulge mass into the disc, conserving the total stellar mass. Nevertheless, a central matter concentration builds up in the case of G1, resulting in the formation of a strong bar (see Fig. 1).

2.2 Simulation technique and numerical parameters

The specific version of GADGET-2 we use includes radiative cooling of the gas and a subresolution multiphase model for the interstellar medium (ISM) that models the effects of star formation and stellar feedback (Springel & Hernquist 2003). Neither black hole accretion nor AGN feedback is included because we want to study highly symmetric galaxies with non-perturbed kinematics, for which black hole growth is expected to be small.

Each galaxy is simulated for a period corresponding to six billion years, with snapshots (i.e. time slices) stored every one hundred million years, which is comparable to the orbital time for particles inside the first few kiloparsecs. This means that there is enough time between snapshots for the galaxy to undergo some small-scale morphological transformations, and therefore we expect our average results not to be strongly biased by odd individual cases with peculiar configurations. We exclude the first seven snapshots of each simulation in order to discard possible transient states during the initial relaxation towards a stable rotational configuration (this can arise because the initial conditions are not in perfect equilibrium);

we then still have a large number of snapshots per galaxy ($\sim$54) in order to identify and explore global trends.

A key parameter in *N*-body simulations is the gravitational softening length, which is meant to keep two-body relaxation effects and orbital integration cost under control. Since gravitational forces are smoothed for particles approaching shorter distances than the softening length, the dynamics of structures smaller than this scale is artificially modified by this approximation. The spatial resolution of an *N*-body simulation is generally considered to be two to three times its softening length. Given that we want to investigate scales as small as 100 pc, we set the softening length to 25 pc in all our simulations. The baryonic particle (i.e. gaseous and stellar particles) masses are chosen to ensure at least eight particles per softening volume within the central 2 kpc inside the disc. The DM particle mass is set to guarantee a minimum of 150 particles inside the inner 100 pc in order to have a relatively smooth DM distribution. Further, we impose an additional constraint, namely $\sqrt{GM_{\rm part}/\epsilon_{\rm soft}} \ll 16\,{\rm km\,s^{-1}}$, which ensures that perturbations induced by two-body encounters are below the typical velocity dispersion of a warm ISM. The resulting baryonic particle masses in our simulations range from $1.2 \times 10^3\,{\rm M_\odot}$ to $1.6 \times 10^4\,{\rm M_\odot}$, and the DM particle masses range from $2 \times 10^4\,{\rm M_\odot}$ to $4 \times 10^4\,{\rm M_\odot}$ (see Table 1).

GADGET-2 uses SPH to solve the hydrodynamic equations of the gas component. This computational method simulates fluids as collections of point-like elements. The SPH technique considers that each gas particle carries a certain amount of every gas property, which is smoothed over a finite volume according to a given kernel function. The value of a quantity at an arbitrary location is given by the sum of the smoothed contributions from all those particles enclosing that point inside their kernel volumes. The kernel employed by GADGET-2 is a spline function with one parameter, the smoothing length *h*, such that the value of every quantity outside a radius *h* is zero. The numerical approximations made in SPH have been shown to be sometimes inaccurate, especially for representing fluid instabilities such as the Kelvin–Helmholtz instability (e.g. Agertz et al. 2007). However, we do not expect that these hydrodynamical accuracy issues have a bearing on the questions studied in this paper, especially because Hayward et al. (2014) found that the results of GADGET-2 simulations of idealized isolated disc galaxies are very similar to simulations of the same galaxies performed with the state-of-the-art moving-mesh hydrodynamics code AREPO (Springel 2010).

3 ANALYSIS METHODS

To fully understand the systematic differences that can arise between the real circular velocity profile of the DM halo and the rotation curve that is actually inferred observationally, one has to go through a long chain of intermediate steps. In order to disentangle the impact of each approximation on the deduced cuspiness of the halo, our general strategy is to apply the same analysis methods to different circular velocity profiles, starting from the most ideal case and adding one layer of approximation at a time. Sorted by the degree of idealization involved, these circular velocity profiles are the following:

  (i) DM-only circular velocity ($V_{\rm dm}$);
  (ii) total-mass circular velocity ($V_{\rm tot}$);
  (iii) true circular motions of the gas ($V_{\rm cir}$);
  (iv) observed rotation curve ($V_{\rm obs}$).

The quantity $V_{\rm dm}$ represents the circular velocity of a test particle under the gravitational potential of the DM halo alone. From a

theoretical point of view, this velocity profile is the only one that traces the exact DM distribution. V_{tot} represents the circular velocity profile generated by the total gravitational potential (i.e. DM plus baryons) in the plane of the disc. With this definition at hand, the minimum disc approximation can be thought of as using V_{tot} instead of V_{dm} to directly estimate the cuspiness of the halo, thus neglecting the baryonic contribution to the potential. In both cases, V_{dm} and V_{tot} do not measure velocities but rather gravitational radial accelerations, as they translate into rotational velocities via $V_{rot}(r) = \sqrt{a_r r}$.

In contrast, V_{cir} is a direct measure for the actual (circular) motions of the gas. Notice that V_{cir} can lie below V_{tot} if the hydrodynamical pressure pushes the gas outwards, thereby lowering the effective radial acceleration towards the centre that needs to be balanced by centrifugal forces. Finally, V_{obs} refers to our mock observed rotation curves, which mimic several processes of real observations, such as projection effects and finite spatial resolution. This generic name comprises a large set of curves for each snapshot because we mimic two types of observations, long-slit rotation curves and 2D velocity fields, at five different inclinations and four different spatial resolutions (to mimic the effect of distance variations). It is worth emphasizing that V_{dm}, V_{tot}, and V_{cir} correspond to perfect theoretical measurements from the simulations, whereas V_{obs} accounts for the limitations of real data. However, we stress that because our simulations are constructed to be highly symmetric discs in perfect rotational equilibrium, even V_{obs} does not fully capture the difficulties inherent in inferring the DM profile shape from observations of real dwarf irregulars and LSB galaxies. Instead, the analysis that we present here should be considered a best-case scenario, at least given current observational limitations.

3.1 Snapshot pre-processing

Before we extract the relevant information from the snapshots, we process them to make sure that the centre of the gravitational potential and the galactic disc orientation are robustly determined. This is very important because poorly constrained values can introduce harmful effects in the forthcoming analysis. For example, note that an error of 5° at low inclinations (~15°) can propagate to an error as high as 50 per cent in the normalization of the observed rotation curves and that an incorrect determination of the centre's position may lead to a spurious flattening of the inner part of a spherically averaged density profile.

We recentre the snapshots using an iterative version of the shrinking spheres method described in Power et al. (2003). We first calculate the centre of mass inside a large sphere containing everything in the simulation and recentre all coordinates around this point. Next, we shrink the sphere by 1 per cent in radius, find the new centre of mass, and recentre the particles again. This is repeated until there are less than 10 particles in the sphere. We also rotate the frame of reference to make the net angular momentum of the gas component coincident with the z-axis.

3.1.1 Real density profiles

To determine the true DM density profiles and verify their steepness, we first measure the DM cumulative mass as a function of radius and then we compute

$$\rho = \frac{\frac{d}{dr} M_{dm}(<r)}{4\pi r^2}.$$ (8)

We use spherical shells equally spaced in logarithmic radius and a central finite-differences scheme for the derivative. We test different steps, namely 0.05, 0.075, 0.1, 0.15, 0.2, and 0.3, and we adopt $\Delta \log(r) = 0.15$, where r is in kpc, which is the smallest interval that produces smooth profiles and is still largely affected by Poisson noise in the central region ($r < 150$ pc). We note that the measured cuspiness of the halo does not depend on this specific choice as variations in the density profiles are very subtle.

3.2 Theoretical circular velocity profiles

We refer to measurements that are calculated from detailed information in the snapshots as theoretical quantities, disregarding the issue of whether or not they can be actually assessed observationally. These quantities include the DM density profiles described earlier as well as a subset of the circular velocity profiles introduced at the beginning of Section 3, namely V_{dm}, V_{tot}, and V_{cir}.

(i) DM-only circular velocity, V_{dm}: particles rotating at a constant speed satisfy $V_{rot}(r) = \sqrt{a_r r}$, so it suffices to determine the mean radial acceleration attributed to the DM halo as a function of radius to determine its equivalent circular velocity profile. To do this, we export all DM particles in the snapshot to a separate initial conditions file and run GADGET-2 for a single time-step to calculate the gravitational forces. Then, we measure the mean radial acceleration in thin spherical shells and compute

$$V_{dm}(r) = \left. \sqrt{\langle a_r(r) \rangle r} \right|_{\text{gravity, dm only}}.$$ (9)

(ii) Total-mass circular velocity, V_{tot}: this velocity profile is related to the gravitational potential of the whole system, i.e. DM plus baryons. It is interesting because a joint analysis with the DM-only circular velocity profile allows one to assess the validity of the minimum disc approximation without mixing in any other effect. Once again, we compute the mean radial accelerations due to gravity using GADGET-2. However, this time we cannot assume spherical but rather axial and vertical symmetries instead. Therefore, we compute the radial accelerations using thin cylindrical shells in the xy-plane ($|z| \leq 100$ pc) and then determine the circular velocity profile using

$$V_{tot}(r) = \left. \sqrt{\langle a_r(r) \rangle r} \right|_{\text{gravity, all particles}}.$$ (10)

(iii) True circular motions of the gas, V_{cir}: in this case, we select the gas particles in the equatorial plane ($|z| \leq 100$ pc) and measure their circular (tangential) velocities, taking the mean value in small radial bins:

$$V_{cir}(r) = \left. \langle V_\phi(r) \rangle \right|_{\text{gas particles}}.$$ (11)

We emphasize that for axisymmetric systems in rotational equilibrium, any difference between V_{cir} and V_{tot} must be due to the fact that in addition to gravity, gaseous media also experience hydrodynamical forces. The above velocity profile is one step closer to reality because instruments do not detect gravitational potentials but rather velocities; thus, V_{cir} can be thought of as the rotation curve that a perfect instrument under perfect observational conditions would detect (neglecting projection effects).

Additionally, we calculate the circular velocity profiles associated with the gravitational potentials of the stellar and the gaseous components separately, using the same procedure as for V_{tot}. These curves are denoted as $V_\star$ and V_{gas} in the text. This complementary information is interesting for understanding the difference between V_{dm} and V_{tot}, as we have that

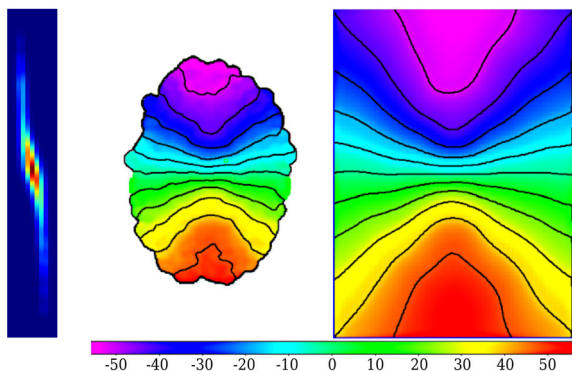$$V_{tot}^2 = V_{dm}^2 + V_\star^2 + V_{gas}^2.$$ (12)

Figure 3. Example data products obtained from G0 at 3.0 Gyr, 45° inclination, and 10 Mpc distance. From left to right, we present the optical long-slit spectrum, the Hα velocity field, and the H I velocity field. The H I velocity map extends over 7 kpc, reaching a maximum radius of 3.5 kpc into the receding and the approaching sides, which is roughly the optical radius. The Hα map barely reaches ∼3 kpc, corresponding to the region with non-negligible emission. Velocities are colour-coded equally in both maps according to the shown scale. Iso-velocity contours are drawn every 10 km s^{-1}. The long-slit spectrum also extends over 7 kpc. Pixels in the horizontal direction represent the spectral axis, coloured according to the intensity of the emission in each velocity channel.

The theoretical rotation curves were calculated using shells of 100-pc width, linearly spaced every 100 pc, the first of which is centred at 125 pc in order to exclude particles inside three times the softening length. Except for when calculating V_{dm}, we only consider particles in the mid-plane because the assumption of vertical symmetry breaks down as one moves above or below the equatorial plane, and this is likely to make particles rotate slower (Rhee et al. 2004). We check that there are a large enough number of particles in all bins, resulting in smooth velocity profiles without visible signs of shot noise. When we explore the effects of spatial resolution associated with the distance to the galaxies, we use re-sampled versions of the theoretical rotation curves matching the radial positions of the corresponding mock observations. The error bars on the theoretical rotation curves are fixed to 1 km s^{-1} where necessary.

3.3 Mock kinematic observations

We mimic different kinds of observations of the gas component, including optical long-slit rotation curves and 2D velocity maps. We consider two different cases, labelled as H I and Hα, which represent some physical properties of the 21-cm and the Hα emissions, respectively. Example data products are shown in Fig. 3.

We *observe* each galaxy at five different inclinations from 15° to 75° in steps of 15°, the smallest one being the closest to a face-on view. We also try four different distances, namely 10, 20, 40, and 80 Mpc. Note that the truly important quantity is the spatial resolution of the observations, but because we use typical values for the instrumental angular resolutions, these distances are useful indicators. For our fiducial Hα point spread function (PSF) of 2 arcsec, the corresponding spatial resolutions are ∼100, ∼200, ∼400, and ∼800 pc. Our H I resolution is six times poorer, but as we use the radio observations only in the outer part of the rotation curves, the optical data are most important for differentiating cusps from cores. In the following, we first describe the basic concepts and common approximations employed to create our mock observations and then move on to more specific details as necessary.

We assume that some of the gas particles emit radiation through a spectrum composed of a single emission line with a Gaussian profile. In the H I case, we consider all gas particles in the simulation to be radio emitters, and we make the amplitude of the 21-cm emission line proportional to the mass of the gas particle. The broadenings are given by the intrinsic velocity dispersions, σ, self-consistently calculated from the temperature of each particle as

$$\sigma = \sqrt{\frac{kT}{\mu m_H}}, \tag{13}$$

where k is the Boltzmann constant, T is the temperature of the gas particle, μ is the mean molecular weight, and m_H is the mass of a hydrogen nucleus. For moving particles, we Doppler-shift the emission line without altering its width. This means that the intensity of the emission from a gas element with a mean velocity $\bar{v}_{los}$ along the line of sight, detected at a different velocity (frequency) v, is given by

$$I_{H I}(v) \propto \frac{M_{part}}{\sigma} e^{-(v-\bar{v}_{los})^2/2\sigma^2}. \tag{14}$$

In the Hα case, we only include gas particles with ongoing star formation activity, which is a good proxy for the spatial distribution of the ionized gas in H II regions, though it may miss the warm ionized gas pervading the rest of the ISM. The mock Hα observations defined in this way have a smaller radial extent than our fiducial mock H I data, consistent with observations. Additionally, the disc of star-forming gas is thinner than our mock H I disc, which makes our choice conservative, as our mock Hα data will be less affected by projection effects and will trace the disc kinematics more faithfully. We make the Hα intensity proportional to the mass of the gas particles times their current star formation rate (SFR), which should roughly correlate with the amount of ionizing radiation available from young, massive stars. The Hα intensity versus frequency is thus given by

$$I_{H\alpha}(v) \propto SFR \times \frac{M_{part}}{\sigma} e^{-(v-\bar{v}_{los})^2/2\sigma^2}. \tag{15}$$

Regarding the observational process itself, we simplify it to a combination of a spatial and a spectral sampling of the emitted radiation field. The spatial sampling mimics the pixels of the detector. To be consistent with the SPH approximation, the radiation flux that a gas particle contributes to a certain pixel is inversely proportional to the projected distance between the particle and the centre of the pixel, using the same kernel and smoothing lengths as in the SPH simulation. Adding contributions from all neighbouring particles, we obtain a resulting spectrum per pixel made up of individual shifted Gaussians. Then, we sample each spectrum in narrow velocity (frequency) channels to mimic the spectral resolution of a given instrument. At the end of this process, we obtain a data cube containing spatial and kinematic information about the gas component in the simulation box. Each slice of this data cube is an intensity map of the Hα or H I radiation in a specific velocity channel. Finally, a 2D Gaussian convolution is implemented across each slice to mimic the effect of the optical seeing or the radio beam, and the cube is collapsed along the spectral axis by means of a simple intensity weighted mean (IWM) scheme to determine the observed line-of-sight velocity at each pixel,

$$\langle v \rangle = \frac{\sum_{ch} I_{ch} v_{ch}}{\sum_{ch} I_{ch}} \tag{16}$$

For the 2D observations, mock intensity and velocity dispersion maps are also generated from the data cubes following Walter et al. (2008)

$$I = \sum_{\text{ch}} I_{\text{ch}} \qquad (17)$$

$$\sigma = \sqrt{\frac{\sum_{\text{ch}} I_{\text{ch}} \times (v_{\text{ch}} - \langle v \rangle)^2}{\sum_{\text{ch}} I_{\text{ch}}}}. \qquad (18)$$

Interesting comparisons of the IWM algorithm with alternative ways of defining a velocity map from its parent data cube are discussed by de Blok et al. (2008) and Oh et al. (2011a). They show that IWM velocities are potentially biased in the presence of non-circular motions as the emission lines become asymmetric or the spectrum may exhibit secondary peaks (i.e. additional velocity components). Notwithstanding, our galaxies are strongly dominated by rotational motions; thus, we find the IWM method good enough to trace the disc rotation. Moreover, we will show in Section 4 that for nearby galaxies, the final results obtained from our mock observations agree remarkably with those obtained from perfect theoretical measurements of the gas kinematics. Therefore, there is no need to employ more complex algorithms than the IWM. The same applies to more sophisticated schemes, as modelling the H I distribution and kinematics directly from the data cubes (e.g. Bouché et al. 2015; Di Teodoro & Fraternali 2015; Kamphuis et al. 2015). Even though a comparison of these methods through our mock data set would be interesting, it lies beyond the scope of this work.

We also address several numerical artefacts detected during the experiments. For example, we noticed that in low-intensity pixels, outliers moving at arbitrary velocities can dominate the velocity estimation and introduce spurious and sometimes enormous fluctuations in the final rotation curve. To avoid this effect, we define an arbitrary luminosity threshold of 10^{-4} times the maximum detected intensity, which works well in suppressing the fluctuations while filtering out just a few pixels. Another potentially harmful effect that we detected is a systematic underestimation of the velocity at the last measured points. We find the main cause of this to be related to the use of the SPH approach, as this implies that in principle, one can define velocities at points that are beyond all gas particles. To remove this artefact, we impose the maximum radius for velocity estimations to be the radius enclosing 99 per cent of the emitting particles. A further comparison between the mock observations and the theoretical rotation curves confirmed that imposing this maximum radius solved the problem. We only report rotation curves for radii beyond 75 pc plus the seeing/beam such that possible contamination from inner points affected by the softening is virtually absent even after the PSF/beam convolution. This places the first kinematic measurement at approximately 0.17, 0.27, 0.46, and 0.85 kpc for galaxies viewed at 10, 20, 40, and 80 Mpc, respectively.

3.3.1 Hα long-slit rotation curves

In this case, we only consider pixels inside a virtual slit placed along the major axis of the disc. We use square pixels and enough spectral channels to sample the whole range of line-of-sight velocities. We choose instrumental parameters consistent with the majority of observational studies. The slit width is 1.4 arcsec, the pixel size is 0.7 arcsec, the full width at half-maximum (FWHM) of the PSF is 2 arcsec, and the spectral resolution is 47 km s^{-1}, equivalent to a 20 km s^{-1} channel separation. The spatial resolution corresponds to ∼100 pc at a distance of 10 Mpc, matching the size of

the radial bins that we used to define the theoretical rotation curves. For mock observations at 20, 40, and 80 Mpc, the corresponding physical resolutions are ∼200, ∼400, and ∼800 pc, respectively. Given that the slit width is resolved into two pixels, we add them together before collapsing the cube to have a single velocity estimate at each position along the slit. Next, we fold the rotation curve to put the approaching and receding sides together, and we average both the radial and velocity information in bins of 1 arcsec (∼50 pc at 10 Mpc), i.e. using two points per seeing, as is common practice for this kind of data. We adopt the standard deviation of individual velocity pixels in the bin as the error bar, and we check that this is perfectly consistent with taking the difference between the approaching and receding sides.

Similar to de Blok & Bosma (2002), we impose a minimum error of 2 km s^{-1} (they used 4 km s^{-1}). Finally, we de-project the observed line-of-sight velocities to get the actual rotation curve,

$$v_{\text{rot}}(r) = \frac{v_{\text{los}}(r)}{\sin(i)}, \qquad (19)$$

where i represents the galaxy inclination. We use the true inclination and major axis of the gaseous disc, and we assume the galactic centre to coincide with the centre of the overall gravitational potential. In a forthcoming paper, we will present mock photometric data of these galaxies and demonstrate that classical photometric estimators can recover the centre of the gravitational potential with an accuracy of 1 arcsec (half the spatial resolution) and the inclination and position angle with typical errors of less than 10°. As we commented in Section 3.1, small inclination errors can induce large differences in the normalization of the rotation curve for discs that are near to face-on. However, it is not clear whether such errors can cause the inferred cuspiness of the halo to be incorrect or they can be safely ignored; regardless, errors of this magnitude would certainly be considered acceptable in actual observational studies. In any case, in this work, we focus on the best case and do not include the effects of errors in the geometrical parameters.

3.3.2 Hα velocity fields

To construct Hα velocity fields, we map the entire Hα emission across the galaxy. The instrumental parameters (pixel scale, seeing, and spectral resolution) are the same as above. The velocity field is computed using the IWM scheme defined in equation (16) and the rotation curves are extracted using the KINEMETRY software package (Krajnović et al. 2006). KINEMETRY performs a harmonic decomposition of the line-of-sight velocity field in elliptical rings as a function of the position angle θ, performing a least-squares minimization of

$$V_{\text{los}}(\theta) = \sum_j A_j \sin(j\theta) + \sum_j B_j \cos(j\theta) \qquad (20)$$

to find the best set of coefficients for each ring. In the case of pure circular motions, we have

$$V_{\text{los}}(\theta) = V_{\text{rot}} \sin(i) \cos(\theta). \qquad (21)$$

Therefore, in the KINEMETRY expansion, the net amount of rotation would be proportional to the coefficient B_1, with all other components representing non-circular motions. We calculate the rotation curves in radial bins of 1 arcsec and adopt as final errors the formal errors of the fit reported by KINEMETRY. Even though KINEMETRY is in principle able to treat the ellipticity and position angle of the ellipses as free parameters during the fitting, we kept them constant and fixed to their real values in order to avoid one additional source of potential error.

3.3.3 H I velocity fields

We also create H I velocity fields following the same prescription. The instrumental parameters are chosen according to the H I survey THINGS (Walter et al. 2008), which, along with LITTLE THINGS (Hunter et al. 2012), represents the best-quality H I data ever used in the cusp–core context. We use a $5.2 \, \text{km s}^{-1}$ channel separation, a pixel scale of $1.5 \, \text{arcsec pixel}^{-1}$, and a Gaussian beam of 12 arcsec at FWHM, such that the spatial resolution is $\sim$580 pc for galaxies at 10 Mpc. Final rotation curves are determined using KINEMETRY in elliptical rings of 6 arcsec width. We note that the spatial resolution of THINGS is better by a factor of 2 in the velocity maps reduced with the robust weighting scheme instead of the natural weighting (see Walter et al. 2008, for details). This fact is exploited to emphasize the advantages of using THINGS velocity maps for cusp–core studies, although it is sometimes not properly stated. For example, Oh et al. (2011a) mentioned the higher spatial resolution in their introduction, but then the poorer resolution ($\sim$12 arcsec) was actually used. This mix-up was propagated into Oh et al. (2011b), in which a spatial resolution of 6 arcsec was used to construct the mock kinematic observations of the simulated galaxies. On the other hand, the data cubes used in those studies had a spectral resolution of $2.6 \, \text{km s}^{-1}$ (a factor of 2 better than ours), but most of the velocity maps in a related study by de Blok et al. (2008) had $5.2 \, \text{km s}^{-1}$ resolution. Regardless, we have checked that measured rotation curves are insensitive to the assumed spectral resolution as long as the Gaussian emission lines are properly sampled.

3.3.4 Hybrid rotation curves

Optical rotation curves have a better spatial resolution than radio observations, but the latter usually cover much larger radii. For this reason, it is very convenient to mix both kinds of data when they are available for the same object, using the Hα measurements in the inner region and appending the H I velocities in the outer part. In this manner, one minimizes concerns about beam smearing while hopefully reaching the flat part of the rotation curve with a high enough number of points in order to put meaningful constraints on the overall shape of the DM halo using rotation curve fitting methods (Section 3.4).

We create hybrid rotation curves by joining the H I data to both the long-slit and the KINEMETRY Hα rotation curves. Given that H I rotation curves are clearly affected by beam smearing in their inner parts, we implemented an automatic algorithm to discard the first H I data points, as needed to get a continuous rotation curve with a positive, monotonically decreasing radial derivative at the Hα/H I interface. The hybrid rotation curves are truncated at $\sim$2 times the optical radius, which is approximated as $\sim$3.2 times the scalelength of the stellar disc (Persic & Salucci 1995), thus yielding radial extents between 5 and 19 kpc, which are representative of real observations.

3.4 Differentiating cusps from cores via rotation curve fitting

When there is kinematic information available beyond the rising part of the rotation curve, the typical method to differentiate cusps from cores is fitting different analytic models to the data set and choosing the best one on the basis of the minimum χ^2_ν of the fits. Amongst the variants presented in the literature, the most common models are the cuspy NFW model (see equations 6 and 7), for which

$\rho_{\text{inner}} \sim r^{-1}$, and the cored pseudo-isothermal sphere (hereafter ISO), for which $\rho_{\text{inner}} \sim r^0$ and the full profile is given by

$$\rho_{\text{ISO}}(r) = \frac{\rho_o}{1 + (r/R_c)^2}, \tag{22}$$

$$v_{\text{ISO}}(r) = \sqrt{\frac{4\pi G \rho_o R_c^3}{r} \left[\frac{r}{R_c} - \tan^{-1}\left(\frac{r}{R_c}\right) \right]}, \tag{23}$$

where ρ_o represents the central DM density and R_c the core radius.

We note that regarding the structure of DM haloes, another criticism of ΛCDM simulations is that the few acceptable NFW fits to observations tend to violate the tight cosmological relation between the free parameters (c, v_{200}) predicted by the simulations themselves. Some authors explicitly use the cosmological mass–concentration relation as a constraint for the NFW fits in order to highlight this additional facet of the cusp–core problem (Kuzio de Naray et al. 2008). We do not impose such a restriction. Instead, we let both parameters vary freely and later investigate the range of values covered by the fits.

When we fit the models to the theoretical velocity profiles V_{dm}, V_{tot}, and V_{cir}, we first re-sample these curves to the same positions at which the mock hybrid rotation curves are measured so that we can properly compare the results and interpret the differences. These radial positions depend on the spatial resolution and the extents of the Hα/H I components of each galaxy. Note that at 10 Mpc, the inner theoretical velocity profiles are oversampled because they were created in steps of $\sim$100 pc, whereas the mock Hα rotation curves are defined every $\sim$50 pc (two points per seeing). However, this is not a concern because we find the results at 10 and 20 Mpc to be essentially identical, as we will show in Sections 4.3 and 5.2. We assume constant error bars of $1 \, \text{km s}^{-1}$ when fitting the theoretical curves.

We recall that this work is focused on the minimum disc approximation; thus, we do not attempt to explicitly account for the baryonic contribution to the rotation curves. In other words, we fit the different analytic models proposed for the DM halo directly to the *observed* data or to the theoretical circular velocity profiles. To avoid spurious results, we do not try fits to rotation curves with less than eight points, which in practice only filters out the velocity profiles from the Dwarf1 and G0 simulations at 80 Mpc.

4 RESULTS

Here, we describe the theoretical velocity profiles of our simulated galaxies, their mock kinematic observations, and some statistics regarding the fits with the NFW and the ISO analytic models. We give special attention to the differences amongst the various velocity profiles and to the effects of spatial resolution and inclination. When reporting on general trends based on observations at all inclinations, we use the term V_{kin} to refer to hybrid rotation curves where the Hα part was extracted with KINEMETRY from the velocity maps, and V_{ls} to refer to those hybrids where the Hα portion uses the mock long-slit data.

4.1 Density profiles

In Fig. 4, we present a compilation of the real DM density profiles in our simulations. Remarkably, we see that our DM haloes
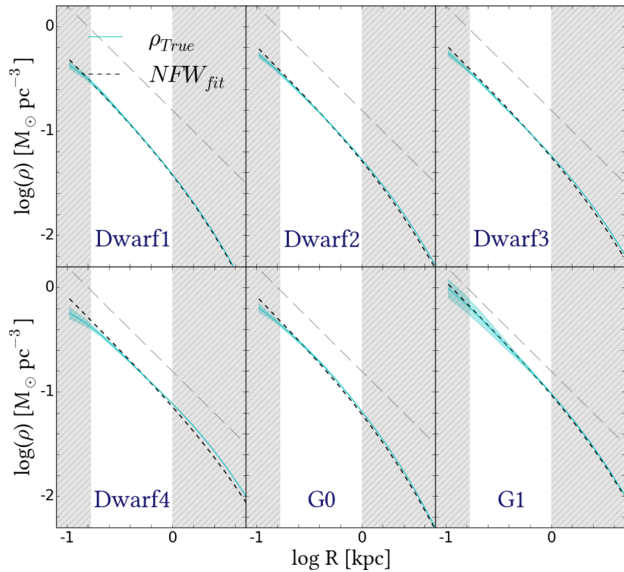
Figure 4. Real DM density profiles in the simulations. The solid cyan lines represent the mean of all the snapshots, and the shaded cyan regions denote the 1σ scatter. In each panel, the short dashed black line is the mean of the best NFW fits to the real density profiles. The hatched, grey shaded regions indicate the central region between 0.17 (the position of our first velocity measurement) and 1 kpc, where the cusp–core discrepancy has been more debated. Straight diagonal lines (long dashed) with a slope of -1 (i.e. the cusp profile expected for an NFW profile) are shown for comparison. All of the simulated galaxies clearly retain central DM cusps throughout their evolution.

remain basically unchanged,[2] even in the case of G1, which develops a relatively strong bar. The simulated galaxies' DM profiles can be accurately represented with the NFW formula, and there is no ambiguity about their cuspy nature. We emphasize this point by including in each panel an inclined straight line with a slope of -1 to facilitate a visual comparison, recalling that a core would appear here as a horizontal line.

4.2 Rotation curves

In Fig. 5, we present a compilation of the theoretical velocity profiles for all galaxies and snapshots. Recall that V_{gas}, $V_{\star}$, and V_{dm} represent the circular velocity profiles generated by the gravitational potential of the individual components, V_{tot} is their sum in quadrature, and V_{cir} is the actual circular speed of the gas in the disc. The negligible scatter demonstrates that our target configurations remain highly stable for all galaxies but G1. Apparently the formation of the bar induces time evolution in the azimuthally averaged velocity profiles, even if the DM structure does not change much. A visual inspection of the face-on stellar maps confirms a smooth,

---

[2] This is likely the case because our simulations use the Springel & Hernquist (2003) effective equation of state to model the effects of supernova feedback and do not include explicit feedback-driven outflows; as a result, the simulated galaxies form stars steadily, in contrast with the very bursty star formation exhibited by simulations that explicitly include multichannel stellar feedback (e.g. Hopkins et al. 2014; Sparre et al. 2015). As detailed in Section 1, strong bursts of star formation and the associated supernova feedback-driven outflows may be able to transform cusps into cores. Thus, it is desirable not to include this still-uncertain effect in our simulations because we wish to test whether cusps can be mistaken for cores, not whether cusps can be transformed into cores via baryonic processes.

stable morphology without substructures for galaxies D1 to D4. Some minor distortions in the central part of G0 are observed, but they are not a concern because the initial potential-velocity structure remains the same. In the following, we present results for the whole sample, excluding G1 at first, and we then comment on this system afterwards.

Fig. 5 shows that baryons are dynamically subdominant in all cases. Inside the first kiloparsec, V_{tot} exceeds V_{dm} by less than $6\,km\,s^{-1}$ for galaxies D1 to D4 and less than $10\,km\,s^{-1}$ for G0. The mean difference $\langle V_{tot} - V_{dm} \rangle$ is less than $3\,km\,s^{-1}$ in this inner region. Beyond the first kiloparsec, the baryonic contribution to V_{tot} is ~10 per cent in galaxies D1, D2, and D3 and ~20 per cent in D4 and G0.

It is also apparent in Fig. 5 that V_{cir} closely follows V_{tot} in the outer region, but it is slightly less than V_{tot} in the centre. The general agreement demonstrates that our systems are in a rotational equilibrium that is mainly sustained by gravity. Nevertheless, as the rotational speed of the gas nearly coincides with the expectation from its radial acceleration (see Section 5.1), the small differences in the centres of the galaxies imply that the radial acceleration experienced by the gas component is smaller than that expected from the gravitational potential, which can be interpreted as evidence for pressure support. The residual ($V_{tot} - V_{cir}$) peaks between 6 and $8\,km\,s^{-1}$ at 0.17 kpc and linearly decreases to ~1–2 $km\,s^{-1}$ at 1 kpc, which implies a mean pressure support correction of ~ 4–5 km s^{-1} to be added to V_{cir} over this radial range. The importance of this small difference in the cusp–core scenario will become clear in the next sections.

In Fig. 6, we present some of the rotation curves and the non-circular motion profiles extracted from the mock Hα and H I velocity maps using KINEMETRY for the simulated galaxies placed at 10 and 80 Mpc and viewed at an inclination of 45°. We also show the theoretical V_{cir} to facilitate the comparison. It is clear from the figure that our galaxies are completely dominated by rotational motions at all radii (except for G1). Fig. 7 shows the mean (taken over all simulations and snapshots) $\langle V_{cir} - V_{kin} \rangle$ residual as a function of spatial resolution for the simulated galaxies viewed from multiple inclinations, considering only the inner region with Hα emission. These figures demonstrate that Hα observations of the simulated galaxies at a 100-pc spatial resolution (placed at a distance of ~10 Mpc) almost perfectly trace the actual circular motions of the gas ($\langle V_{cir} - V_{kin} \rangle < 2\,km\,s^{-1}$). The residual increases as the spatial resolution diminishes and reaches as much as ~5 km s^{-1} for a 800-pc resolution (~80 Mpc distance) and inclination of 15°. The H I rotation curves (the red lines in Fig. 6) underestimate the true rotational velocities in the central few kiloparsecs of the galaxies (even when the galaxies are placed at 10 Mpc) but are in agreement with V_{cir} at larger radii. The effect of beam smearing is stronger with distance, but because we use the H I data only to extend the optical rotation curves into the flat part, this is not a primary concern for our discussion.

G1 qualitatively differs from the other simulations. In this simulation, the stellar component dominates the gravitational potential within the first 2 kpc. As a result, V_{tot} exceeds V_{dm} by $27 \pm 5\,km\,s^{-1}$ at 1 kpc (see Fig. 6), which represents a discrepancy of ~50 per cent. In the outer region, this excess is about 30–40 per cent. The residual ($V_{tot} - V_{cir}$) is $15 \pm 5\,km\,s^{-1}$ at 0.17 kpc, $8 \pm 5\,km\,s^{-1}$ at 1 kpc, and 2 km s^{-1} at ~2.5 kpc. However, in this case, the difference is not simply attributable to the effect of pressure support because of the presence of the bar and its associated non-circular motions, which invalidate the axisymmetric approximation. We emphasize that G1 resembles classical dwarf galaxies and LSBs in terms
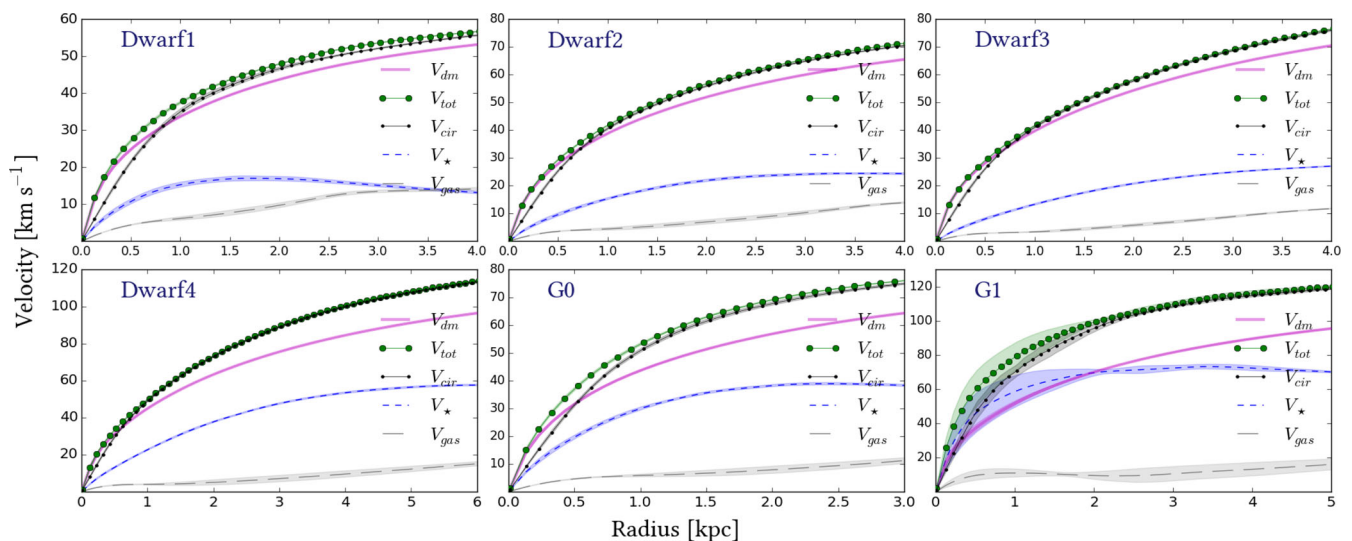
Figure 5. Inner parts of the theoretical rotation curves as defined in Section 3. The thick magenta line represents V_{dm}, solid green line with circles is V_{tot}, solid black line with dots is V_{cir}, the short-dashed blue line is $V_\star$, and long-dashed grey line is for V_{gas}. In each case, the main line is the mean curve from all snapshots, and the shaded regions indicate the 1σ scatter. Except for G1, the simulated galaxies are DM dominated at all radii. The differences between V_{tot} and V_{cir} in the central ~ 1 kpc, which are typically ~ 4–5 km s^{-1}, are due to pressure support; below, we shall see that this difference can have important consequences for the DM profile shape inferred from the rotation curves.
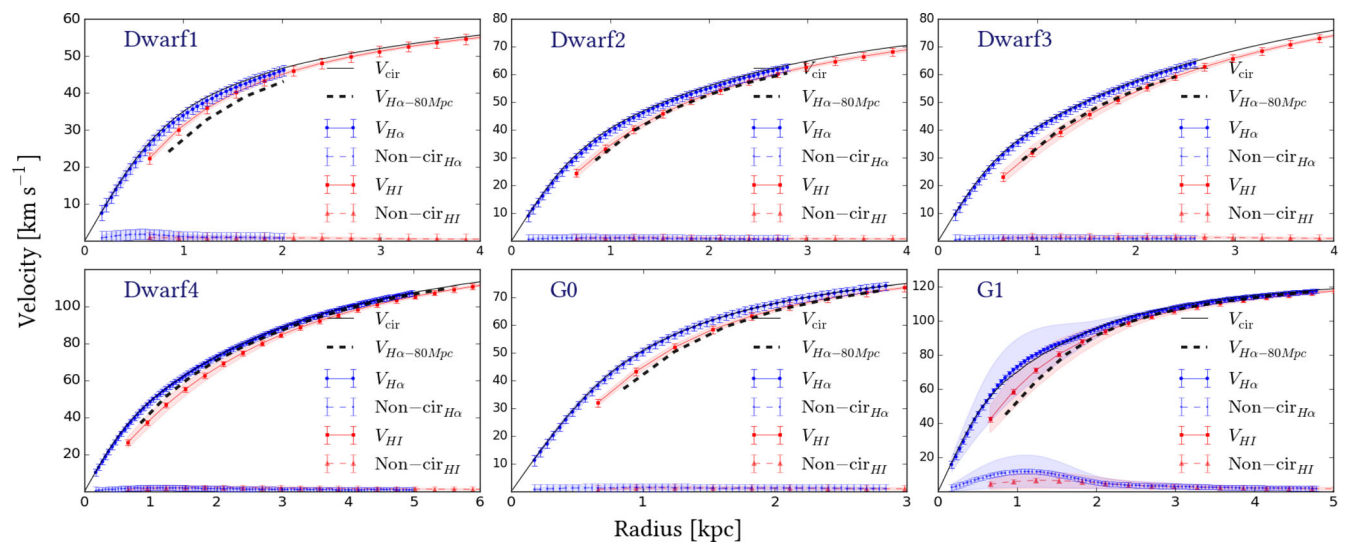

Figure 6. Inner parts of the mock observed rotation curves and net amount of non-circular motion as inferred by KINEMETRY for the simulated galaxies placed at 10 Mpc and viewed at an inclination of 45°. Hα observations appear in blue and H I in red. In each case, the rotation curve is represented with a solid line and the non-circular motion profile with a dashed line. For each of the above, the plotted curve represents the mean curve from all snapshots, the shaded region indicates the 1σ scatter, and the error bars represent the typical error bar at each radius on individual rotation curves. The theoretical V_{cir} is also shown. The thick black dashed line in each panel is the Hα rotation curve at 80 Mpc. The rotation curves are dominated by circular motion at all radii. The Hα rotation curves almost perfectly trace the true circular motions of the gas for galaxies placed at 10 Mpc but underestimate them by as much as ~ 5 km s^{-1} when the galaxies are placed at 80 Mpc (and even more so for G1 because of the non-negligible amount of non-circular motion in the central 2 kpc). The H I rotation curves underestimate the true circular velocity in the central few kiloparsecs because of beam smearing.

of several properties, such as the maximum circular velocity and stellar mass; for this reason, we keep it in our sample even though it is not close to the ideal case. Modelling the complex kinematics of barred potentials is far from simple and beyond the scope of this work.

The mock Hα rotation curves obtained from the 2D velocity maps underestimate the circular motions of the gas more severely in less-inclined (i.e. more face-on) galaxies. Despite the differences being small, they are systematic, as shown in Fig. 7. On a case-by-case basis, some scatter and random small-scale fluctuations are

visible. In particular, the rotation curves for galaxies viewed at an inclination of 15° often exhibit prominent shape distortions that are not seen at other inclinations.

We find the same trend with spatial resolution but not with inclination in the mock long-slit data. In this case, the rotation curves of galaxies viewed at an inclination of 75° exhibit the most underestimated circular velocities, followed by galaxies at 15°; for other inclinations, the long-slit rotation curves are effectively independent of inclination (see Fig. 7). The long-slit rotation curves are a bit noisy and exhibit more scatter than those from the 2D velocity
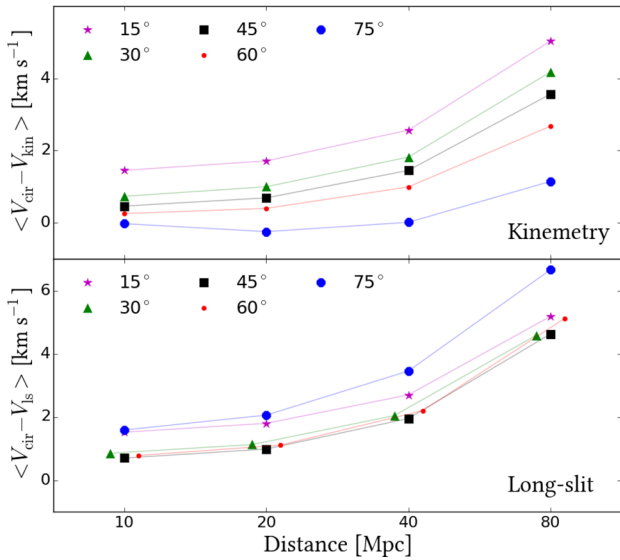
Figure 7. Mean Hα velocity residuals $\langle V_{cir} - V_{kin} \rangle$ (top), and $\langle V_{cir} - V_{ls} \rangle$ (bottom) as a function of distance (spatial resolution) and inclination for all galaxies and snapshots. Some markers are slightly shifted horizontally to make the plot more readable. The residual increases as the spatial sampling gets coarser, reaching as much as ~5 km s⁻¹. The rotation curves from the KINEMETRY analysis exhibit larger residuals when the galaxies are viewed more face-on. In the long-slit case, the largest residual occurs in discs inclined at 75°.

maps, mainly at low inclinations and high spatial samplings (small distances). Nevertheless, the average difference $\langle V_{cir} - V_{ls} \rangle$ is comparable to the previous case. The only exception is G1 viewed at an inclination of 75°, for which the average velocity underestimation at 80 Mpc increases to ~11 km s⁻¹ because of the galaxy's lack of symmetry during the second half of the simulation.

4.3 Rotation curve fitting

In Fig. 8, we compare the reduced χ_ν^2 of the best-fitting NFW and ISO models for the various types of rotation curves for the D2 simulation placed at 10 Mpc. This is a good example of the general trends in the whole sample, so we use it to introduce our main findings before going into a more detailed analysis.

Points that lie below the one-to-one line in Fig. 8, represent better agreement of the data with the NFW model, and points above the diagonal indicate that the ISO model provides a better description of the data. We see that the NFW profile fits the theoretical V_{dm} and V_{tot} curves much better, as expected because by construction the central potential of the galaxy is dominated by the DM, which obeys an NFW profile. The results from fitting V_{tot} are somewhat closer to the line of equality between models than those from V_{dm} because of the effect of the baryonic contribution to the rotation curve. Surprisingly, V_{cir} is better fit by the ISO model than by the NFW model. The fits to the mock rotation curves tend to favour the ISO model, especially when the galaxies are viewed at high inclinations.

We now discuss the results for all of the galaxies and snapshots. In Fig. 9 and Table 2, we show the fraction of cases in which one of the models is preferred over the other for each type of circular velocity profile.[3] We estimate a lower limit on these fractions by
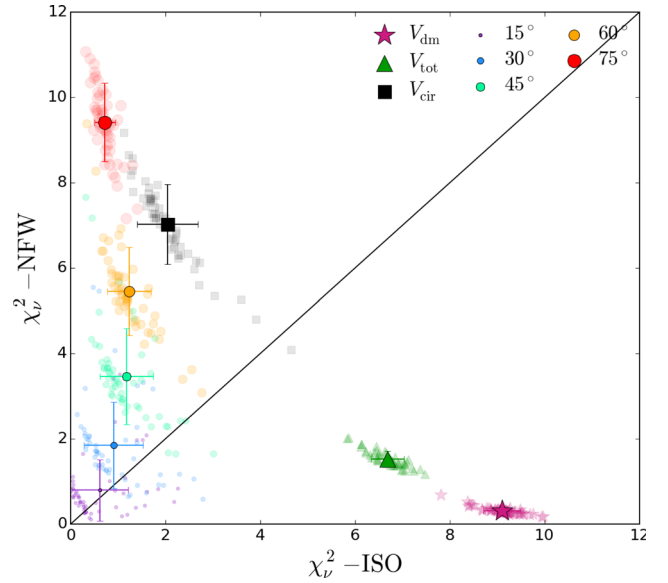
Figure 8. Distribution of χ_ν^2 obtained by fitting the NFW and ISO models to the various types of rotation curves for the Dwarf2 simulation placed at 10 Mpc. The shapes, colours, and sizes of the markers are coded according to the specific rotation curve used, as detailed in the legend. Background semitransparent symbols correspond to the results for individual snapshots, the solid symbols in the front denote the centroids of the corresponding clouds of points, and the error bars represent the 1σ scatter in the horizontal and vertical directions. The black diagonal line represents equality between the goodness of the fits. For this simulation, the theoretical rotation curves V_{dm} and V_{tot} are better fit by the cuspy NFW model. However, the theoretical rotation curve V_{cir} is better fit by the ISO model because pressure support causes V_{cir} to be less than V_{tot} in the central ~1 kpc. The mock rotation curves obtained using KINEMETRY are generally better fit with the ISO model, especially when the galaxies are viewed at inclinations of 45° or greater. These results demonstrate that rotation curve fitting can indicate the presence of a core when the true DM profile is cuspy.

demanding one χ_ν^2 to be at least 1.5 times smaller than its counterpart and stating that both models are equally good otherwise. For this reason, the sum of the NFW and ISO fractions is not always unity. Upper limits are obtained by relaxing our threshold on the χ_ν^2's ratio from 1.5 to 1.1. We find 100 per cent of the V_{dm} rotation curves to be better represented by the cuspy NFW model for all the tested spatial samplings (≤400 pc for $D \leq 80$ Mpc), in perfect agreement with the underlying DM distributions in the simulations.

Using V_{tot}, we find that between 52 and 61 per cent of the rotation curves are better fit with the NFW profile, whereas between 35 and 39 per cent of the cases are better fit by the ISO model. This means that the signature of the NFW haloes is still detectable, although the inclusion of the baryonic contribution to the potential without an explicit correction during the fit introduces considerable errors. In particular, we note that the NFW model is always better for D1, D2, and D3, but it is disfavoured for D4 and G0. In the case of G1, both models provide comparable fits to V_{tot}. Strikingly, the V_{cir} rotation curves for simulated galaxies viewed at $D \leq 40$ Mpc, i.e. whose inner parts are sampled every ≤200 pc, are better fit with the

---

[3] We remind the reader that the theoretical rotation curves (V_{dm}, V_{tot}, and V_{cir}) are resampled to the same positions of the mock observations; con-

sequently, the results depend on the assumed distance. Also recall that we observe the curves at a rate of two points per seeing. So, at a distance of 80 Mpc, the spatial resolution of the mock observations is ~800 pc, but they are sampled at a rate of ~1/400 pc⁻¹, and this is what matters for the theoretical velocity profiles.
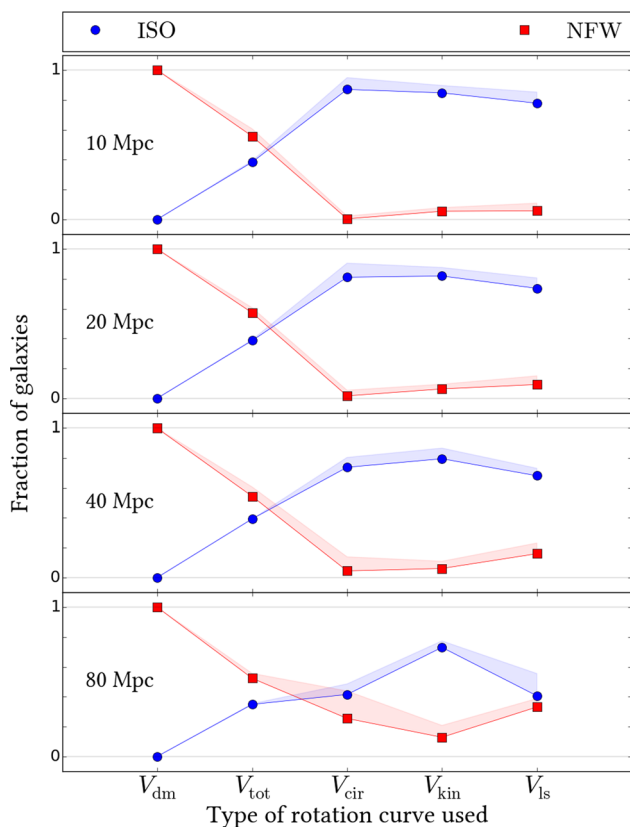
Figure 9. Fraction of galaxies that are better represented by the NFW or ISO models based on the best-fitting χ_ν^2 values. Solid lines are established by demanding that one of χ_ν^2 values is at least 1.5 times bigger than the other one. The upper limit of the shaded regions represents the upper limits on the NFW/ISO fractions, which were obtained using a threshold of 1.1 instead of 1.5. $V_{\rm dm}$ is always better fit by the NFW model, as expected because the DM profiles of the simulations obey an NFW profile. In contrast, $V_{\rm tot}$ is sometimes better fit by the ISO model because of the baryonic contribution to the potential. In the vast majority of cases, the cored ISO model provides a better fit to the theoretical circular velocity profile $V_{\rm cir}$ and the mock rotation curves, despite the simulations containing cuspy DM profiles by construction.

ISO model for 74–95 per cent of the sample. Such a result would be typically interpreted as proof of the ubiquitous presence of cores in the central region of galactic haloes, but because there are no cores in our simulations, this conclusion would be incorrect. This fact is particularly shocking because $V_{\rm cir}$ is a perfect theoretical measurement of the gas rotational velocity, and it occurs even when the galaxies are viewed at 10 Mpc (i.e. the spatial resolution is optimal). When viewed at 80 Mpc, the difference between models decreases, although the illusion of DM cores does not vanish entirely; the NFW profile is preferred in 25–44 per cent of the cases, and the ISO model provides a better fit in 42–49 per cent of the cases.

Regarding the mock observations and considering all distances and inclinations, the ISO model provides a better fit to $V_{\rm kin}$ for 73–90 per cent of the sample, and the NFW model is preferred for only 5–21 per cent of the sample. Thus, this type of analysis applied to our observed rotation curves would provide strong evidence of the widespread existence of cores in the DM haloes of dwarf galaxies and LSBs, which is in tension with the cuspy nature of the DM haloes in our simulations. This effect is more misleading for more nearby galaxies. It is worth emphasizing that whatever the reason for the ISO model being a better fit to the mock observations, the

Table 2. Percentages of rotation curves that are better represented by the NFW or ISO models according to the type of rotation curve and the spatial resolution (assumed distance).

Hα PSF (pc)		~100	~200	~400	~800
D (Mpc)		10	20	40	80
$V_{\rm dm}$	NFW	100 (100)	100 (100)	100 (100)	100 (100)
	ISO	0 (0)	0 (0)	0 (0)	0 (0)
	Both	0 (0)	0 (0)	0 (0)	0 (0)
$V_{\rm tot}$	NFW	56 (61)	57 (61)	54 (61)	52 (56)
	ISO	38 (39)	39 (39)	39 (39)	35 (35)
	Both	6 (0)	4 (0)	6 (0)	13 (9)
$V_{\rm cir}$	NFW	0 (2)	2 (5)	4 (14)	25 (44)
	ISO	87 (95)	81 (91)	74 (81)	42 (49)
	Both	13 (3)	17 (4)	22 (6)	33 (8)
$V_{\rm kin}{}^a$	NFW	5 (8)	6 (9)	6 (11)	13 (21)
	ISO	85 (90)	82 (88)	80 (87)	73 (77)
	Both	10 (2)	12 (3)	14 (2)	14 (2)
$V_{\rm ls}{}^a$	NFW	6 (11)	9 (15)	16 (23)	33 (39)
	ISO	78 (85)	74 (81)	68 (73)	41 (56)
	Both	16 (4)	17 (4)	16 (4)	26 (6)

Note. The fiducial NFW/ISO fractions are estimated by demanding that one of the χ_ν^2 values to be at least 1.5 times smaller than the other one. Values in parentheses require a minimum ratio of 1.1 between the χ_ν^2 values. The rows labelled 'Both' correspond to cases for which the χ_ν^2 values of the NFW and ISO fits differ by less than a factor of 1.5 (1.1).
^{a}The values for $V_{\rm kin}$ and $V_{\rm ls}$ are for the mock rotation curves at all inclinations.

effect is already evident when we analyse the theoretical circular motions of the gas, $V_{\rm cir}$. We note the same trend in the results from long-slit data as for the 2D velocity maps. The only difference occurs at 80 Mpc, where the ISO model is preferred by a much smaller margin and the number of unresolved cases is larger when the long-slit rotation curves are used.

In Fig. 10 and Table 3, we categorize the results from the 2D mock observations according to the inner spatial resolution and inclination. We see that the NFW profile is virtually never preferred when the galaxies are viewed at an inclination of 75°. Considering specific combinations of distance and inclination, we see that the NFW model sometimes provides better fits, but these are limited to a maximum of 24 per cent of the sample, whereas the ISO profile fits the data better in 65–100 per cent of the cases. In Fig. 10, note that the blue (ISO) and red (NFW) regions never overlap, reflecting the fact that the fraction of rotation curves that are better fit with the ISO model is always greater than the fraction better fit with the NFW model. The difference between the two fractions increases with inclination. Finally, we note that the gap between the coloured stripes becomes narrower at 80 Mpc, as the sampling gets poorer.

In Fig. 11 and Table 4, we repeat the exercise for the long-slit data. At 10 Mpc (~100-pc inner spatial resolution), we see the same trend with inclination as before, i.e. more inclined galaxies appear more cored. This tendency becomes weaker at 20 Mpc, and it does not hold beyond that. Regarding the trend with distance, the ambiguity between models increases more rapidly compared with when the 2D velocity maps were used. In particular, when the galaxies are placed at 80 Mpc, of order half the sample appears to contain cores and a major fraction of the other half appears to contain cusps. Finally, it is worth noting that these general results are not biased by the inclusion of G1, i.e. they do not change substantially if we exclude this simulation.
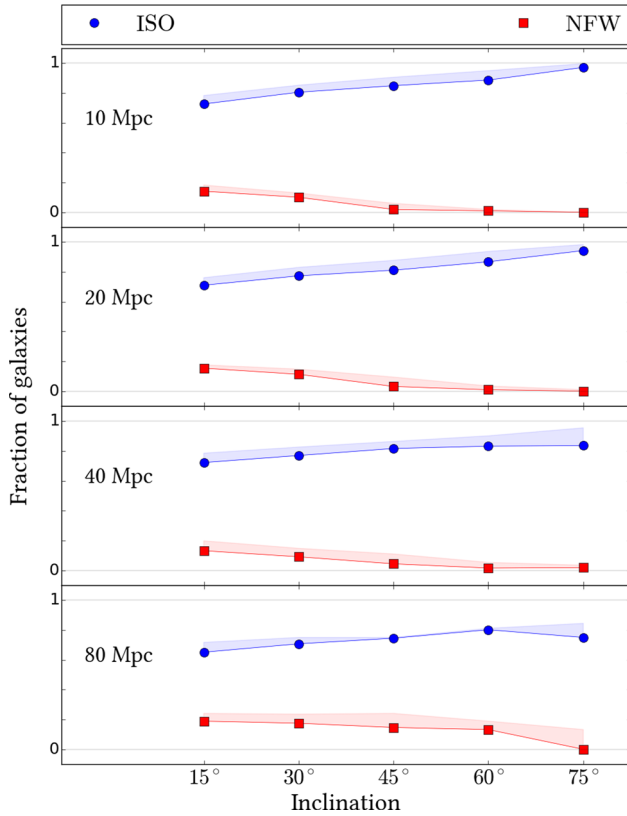
Figure 10. Fraction of mock rotation curves that are better described by the NFW/ISO models as a function inclination for the mock 2D observations analysed with KINEMETRY. The different rows correspond to different assumed distances (from top to bottom: 10, 20, 40, and 80 Mpc). The symbols and colours are the same as in Fig. 9. Independent of inclination and distance, the rotation curves derived from the 2D velocity maps are always better fit by the cored ISO model than by the cuspy NFW model.
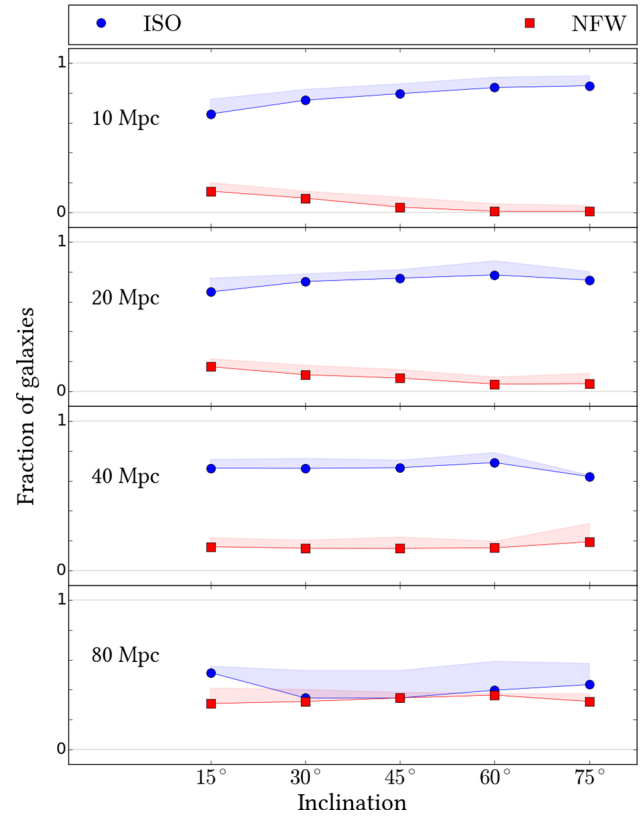
Figure 11. Fraction of mock rotation curves that are better described by the NFW/ISO models as a function of distance and inclination for the hybrid rotation curves using mock Hα long-slit data. The symbols and colours are the same as in Fig. 9. Except for an assumed distance of 80 Mpc, the ISO model is incorrectly preferred in the majority of cases. For 80 Mpc, of order half of the rotation curves are better fit with the cored ISO model despite the galaxies having cuspy profiles.

Table 3. Similar to Table 2, but for the rotation curves obtained by analysing the mock 2D velocity maps with KINEMETRY (V_{kin}) and classified according to the assumed distance and inclination.

Hα PSF (pc)	~100	~200	~400	~800
D (Mpc)	10	20	40	80
15° NFW	14 (18)	15 (18)	13 (20)	19 (24)
ISO	73 (78)	71 (76)	72 (79)	65 (72)
Both	13 (3)	14 (6)	14 (2)	16 (4)
30° NFW	10 (13)	11 (15)	9 (15)	17 (24)
ISO	81 (85)	77 (83)	77 (83)	71 (75)
Both	9 (2)	11 (2)	14 (3)	12 (1)
45° NFW	2 (6)	3 (9)	4 (11)	15 (24)
ISO	85 (91)	81 (88)	82 (86)	75 (75)
Both	13 (3)	16 (3)	14 (3)	11 (1)
60° NFW	1 (2)	1 (3)	2 (5)	13 (19)
ISO	89 (95)	87 (94)	83 (90)	80 (81)
Both	10 (3)	12 (3)	15 (4)	7 (0)
75° NFW	0 (0)	0 (1)	2 (3)	0 (13)
ISO	97 (100)	94 (98)	84 (96)	75 (84)
Both	3 (0)	6 (1)	14 (1)	25 (2)

Table 4. Similar to Table 2 but for V_{ls}, the hybrid rotation curves using the mock Hα long-slit data, classified according to the assumed distance and inclination.

Hα PSF (pc)	~100	~200	~400	~800
D (Mpc)	10	20	40	80
15° NFW	14 (20)	16 (22)	16 (22)	31 (41)
ISO	66 (76)	67 (76)	69 (74)	51 (56)
Both	20 (4)	17 (3)	16 (4)	18 (3)
30° NFW	9 (14)	11 (17)	15 (20)	32 (40)
ISO	75 (82)	74 (79)	68 (75)	34 (53)
Both	15 (3)	15 (4)	17 (5)	33 (7)
45° NFW	3 (10)	9 (14)	15 (22)	34 (38)
ISO	80 (86)	76 (81)	69 (74)	34 (53)
Both	17 (4)	15 (4)	16 (4)	31 (9)
60° NFW	1 (6)	5 (9)	15 (19)	36 (37)
ISO	84 (91)	78 (87)	72 (79)	40 (59)
Both	16 (4)	17 (3)	13 (2)	24 (4)
75° NFW	1 (4)	5 (12)	19 (31)	32 (37)
ISO	85 (92)	75 (80)	63 (64)	43 (58)
Both	14 (4)	20 (8)	18 (5)	25 (5)

5 DISCUSSION

So far we have presented strong evidence that rotation curve fitting can yield qualitatively incorrect conclusions regarding the inner curvature of the density profiles of galactic DM haloes. Here, we discuss the origin of the errors based on the differences amongst the theoretical velocity profiles, check the dependence of the results on the radial range covered by the rotation curves, and compare the coefficients of our best fits to a collection of results from the literature to demonstrate that our mock observed rotation curves are in fact representative of real galaxies. We also compare our main findings against other works which analysed synthetic observations from numerical simulations in the cusp–core context.

5.1 Unravelling the illusion of DM cores

First, we focus on the real shapes of the different velocity profiles, i.e. we refer to rotation curves of simulated galaxies placed at 10 Mpc, for which the spatial resolution is high (∼100 pc). The explicit effect of poorer spatial resolution is commented on in Section 5.2. We recall that 100 per cent of the $V_{\rm dm}$ profiles are better described by the NFW model. Consequently, in principle, rotation curve fitting can recognize a cuspy DM distribution from its true circular velocity profile given sufficient spatial sampling (≤400 pc).

As for $V_{\rm tot}$, we have seen that NFW profiles are more favoured in the sample as a whole, although the ISO model fits the velocity profiles from D4 and G0 better, and for G1, the two models provide superior fits for similar fractions of the rotation curves. Additionally, for D1, D2, and D3, the confidence with which the rotation curve fitting detects the cuspy haloes, as judged based on the χ^2_ν values of the fits to $V_{\rm tot}$, is somewhat reduced compared with $V_{\rm dm}$. These results challenge the widespread assumption that the contribution of baryons to the potential will tend to make the DM profile inferred under the minimum disc assumption cuspier than the true DM profile.[4] These results also imply that the minimum disc approximation is unacceptable for some dwarf galaxies. To better understand this result, in Fig. 12 we plot the inner velocity profiles expressed as fractions of $V_{\rm tot}$. Noting that the circular velocity profile of a spherical halo is given by the enclosed mass as a function of radius, which can be estimated from the density profile by integration, it can be shown that $\rho_{\rm inner} \propto r^0$ cores result in linear inner circular velocity profiles, $v_{\rm inner} \propto r^1$, whereas $\rho_{\rm inner} \propto r^{-1}$ NFW cusps lead to $v_{\rm inner} \propto r^{0.5}$. In other words, cuspier density profiles produce more curved velocity profiles characterized by smaller exponents, but always inside the interval [0.5, 1] for the limits we are considering. Because the fraction $V_{\rm dm}/V_{\rm tot}$ systematically decreases with radius, this quotient has a negative exponent when expressed as a power law, which implies that the exponent of $V_{\rm tot}$ is larger (closer to 1) than that of $V_{\rm dm}$. Consequently, the DM distributions inferred from $V_{\rm tot}$ are less cuspy than those inferred from $V_{\rm dm}$. In other words, the contribution of baryons to the potential tends to make the circular velocity profile flatter rather than cuspier. This result may not hold for all galaxies, but the salient point is that there is no justification to claim a universal ability of the minimum disc approximation to make the inferred DM density profiles appear cuspier than they truly are. More likely, the resulting cuspiness of $V_{\rm tot}$ will depend on the relative curvatures and normalizations of the dark and luminous components. Also note that in Fig. 12, the

inner, negative slope of the $V_{\rm dm}/V_{\rm tot}$ profile is shallower in D1, D2, and D3 than in the other simulations, and these simulated galaxies have the smallest baryonic-to-DM ratios amongst our sample. Consequently, the inner curvatures of $V_{\rm dm}$ and $V_{\rm tot}$ must differ the less in these galaxies.

In the case of $V_{\rm cir}$, the rotation curve fitting analysis is completely misleading because the cored ISO model provides better fits to most of the rotation curves. Thus, the core-like shape that we infer from the mock rotation curves is already imprinted in $V_{\rm cir}$ and is therefore not (only) a consequence of observational errors (e.g. projection effects). Fig. 12 provides insight into this issue. We see that in all galaxies, $V_{\rm cir}$ is approximately ∼50 per cent of $V_{\rm tot}$ in the very centre and progressively increases until it reaches a fractional contribution of order unity just outside the first kiloparsec. This systematic trend is opposite to the one that we found in the case of $V_{\rm dm}$ and necessarily implies that the inner curvature of $V_{\rm cir}$ is much less pronounced than that of $V_{\rm tot}$ (i.e. the mass distribution inferred from $V_{\rm cir}$ is much less cuspy than the mass distribution inferred from $V_{\rm tot}$).

Why is $V_{\rm cir}$ typically less than $V_{\rm tot}$, especially at small radii? Our tests indicate that it is the result of pressure support, i.e. an effective decrease in the radial acceleration because of an outward force of the gas on itself, which is the result of a negative radial pressure gradient. To illustrate this point, we include in Fig. 12 the circular velocity corresponding to the radial acceleration experienced by the gas component, i.e. $\sqrt{a_{r_{\rm gas}} r}$, which closely corresponds to the actual circular velocity of the gas, $V_{\rm cir}$. This correspondence demonstrates that the gas component is in rotational equilibrium but also shows that within the first kiloparsec, the radial acceleration experienced by the gas particles is less than that experienced by the stellar ones (which is used to define $V_{\rm tot}$). Because the overall gravitational potential is the same for gas and stars, the only physical phenomenon we identify that is capable of causing the difference is pressure support associated with the high gas density in the galactic centres and the injection of thermal energy from stars into the ISM. In Section 5.5, we present further evidence in this regard and address the (im)possibility of accurately correcting the mock rotation curves for pressure support using observationally accessible information.

Regarding the mock observations, we know that for galaxies placed at 10 Mpc, the mock rotation curves perfectly follow the theoretical $V_{\rm cir}$ curve (Fig. 6); thus, their cored shapes simply reflect the curvature of the true circular motions of the gas, as determined by the full hydrodynamics and not only by gravity. Moreover, a careful inspection of Fig. 9 reveals that the gap between the ISO and NFW fractions is less for $V_{\rm ls}$ than for $V_{\rm kin}$. After a thorough review of the fitting procedure, we concluded that this difference is a result of the size of the error bars, which are larger for the long-slit observations than for the rotation curves obtained from the 2D velocity maps with KINEMETRY. Consequently, the individual points of the mock Hα long-slit rotation curves, which determine the inner curvature of the profiles, have a smaller weight during the fits than the outer points from the mock H I rotation curves, thus reducing the significance of the core detections.

5.2 Dependence on spatial resolution and inclination: beam-smearing and projection effects

Recalling that our theoretical rotation curves for galaxies at $D >$ 10 Mpc are simply re-sampled versions of the 10-Mpc curves and noting that the NFW model fits better all the $V_{\rm dm}$ profiles independent of distance, we conclude that rotation curve fitting methods can distinguish the signature of an ideal cuspy NFW profile even at

---

[4] This is usually expressed in other words, i.e. stating that the minimum disc approximation puts an upper limit on the steepness of the DM halo density profile (e.g. de Blok et al. 2001).
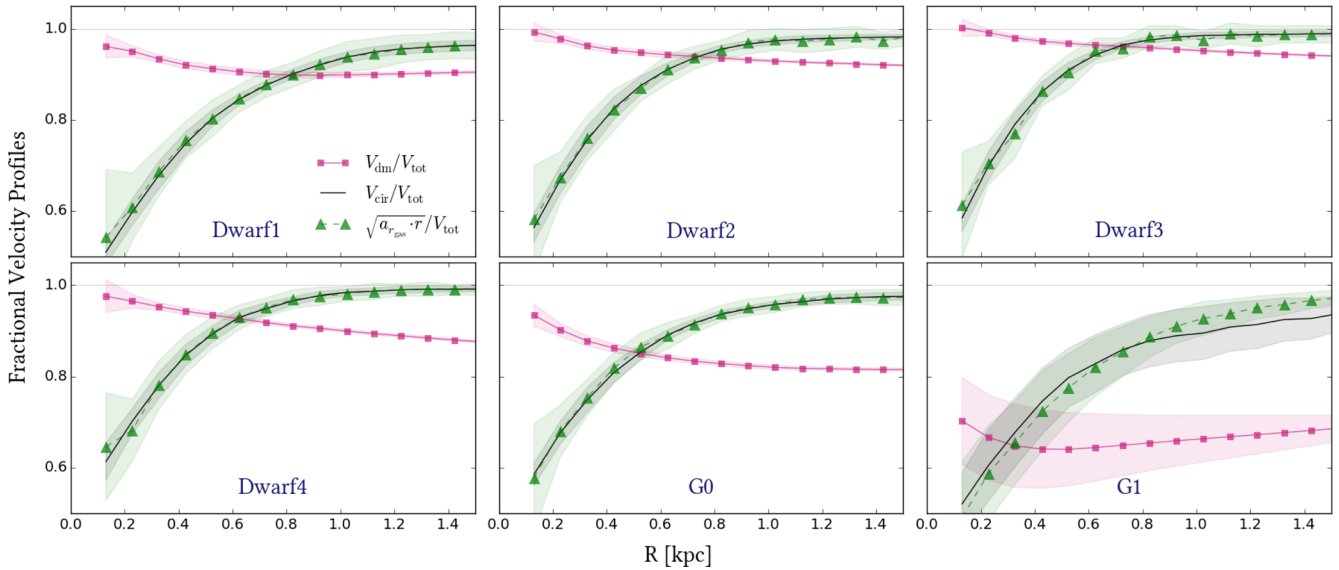
Figure 12. Theoretical velocity profiles within the central 1.5 kpc expressed as a fraction of V_{tot}. Black solid line is for V_{cir} and magenta solid line with square markers for V_{dm}. In addition, we show with green triangles joined by a dashed line the velocity profiles inferred from the radial acceleration of the gaseous particles in our simulations, i.e. $\sqrt{a_{r_{gas}} r}$. Each line represents the mean taken over all snapshots, and the shaded regions represent the 1σ scatter amongst snapshots. The fact that V_{dm}/V_{tot} decreases with radius implies that the DM profile is cuspier than the total mass profile and thus the minimum disc assumption does not place an upper limit on the cuspiness of the DM profile. Moreover, both V_{cir} and the circular velocity corresponding to the radial acceleration experienced by the gas component, which are almost identical, are generally less than V_{tot} because of pressure support, and the fractional difference is greater at smaller radii. This systematic behaviour implies that the matter distribution inferred from V_{cir} will look flatter than that inferred from V_{tot}.

a sampling rate of ∼400 pc in the rising part (1 arcsec at 80 Mpc) with the first measurement at ∼0.9 kpc, at least for the (c, v_{200}) parameter space covered by our models.

The situation is a bit different for cores. We know from the former sections that the intrinsic shape of V_{cir} is close to the ISO profile, which is favoured in more than 80 per cent of the fits for galaxies placed at 10 Mpc. However, the fraction of cores steadily declines as the galaxies are placed further away, with a simultaneous increase in the number of preferred NFW fits and ambiguous cases. At 80 Mpc, the number of galaxies catalogued as cusps is comparable to the number of galaxies catalogued as cores. This is partially explained by the small sizes of the fake cores (∼1 kpc), whose signature is progressively washed out as the sampling gets poorer and the first measured point moves to larger radii. Yet we note that this is only true for D2, D3, and mildly for G1. Fits to V_{cir} in the other galaxies favour the ISO model at all distances, showing that the outcome of the fits depends on more subtleties than just the sampling rate.

It is important to note that undersampling the curves is not sufficient to fully model the impact of spatial resolution. Beam smearing, i.e. the smoothing of the velocity gradients in the rising part of the rotation curves caused by averaging over large PSF/beam areas, is also a resolution effect. The measured velocities are further lowered by projection effects related to the fact that, in inclined discs of finite thickness, any line of sight targeting an inner position mixes information from tracers at larger radii, whose line-of-sight velocity component is very small because of the inherent geometry of the rotating disc (Rhee et al. 2004). Note that the volume of gas crossed by a single telescope pointing increases as the spatial resolution becomes coarser and as the galaxy inclination and disc thickness are increased; thus, in order to assess these entangled effects properly, we must confront our mock kinematic observations with the theoretical velocity profiles.

Comparing the results from V_{kin} with those from V_{cir} (Fig. 9), we see that they are very similar at $D \leq 40$ Mpc, i.e. the effect of

beam-smearing and projection effects is mild for inner spatial resolutions ≤400 pc, though they effectively introduce the dependence with inclination discussed in Section 4.3. At 80 Mpc, in contrast, beam-smearing and projection effects cause a significant difference between the results from V_{kin} and V_{cir}, as a large fraction of the mock observations are better explained by a cored profile. In this case, the signature of the fake core does not vanish with the poor sampling in any case because the additional effects considerably lower the inner measured velocities, thereby reinforcing the illusion of a DM core (Fig. 6).

As can be seen in Fig. 9, the effect of distance on V_{ls} is to progressively reduce the fraction of cases that are better fit by the ISO model, while augmenting those which are better fit by the NFW profile. The increasing ambiguity, which is more noticeable than in the case of V_{kin}, results from the larger size of the Hα long-slit error bars in comparison to the H I error bars reported by KINEMETRY and illustrates the sensibility of the rotation curve fitting analyses to the specific details in the treatment of the data. Using V_{ls}, we only observe systematic effects with inclination at 10 and 20 Mpc; we suspect that they are strongly dependent on the existence of inner measurements and their relative weights during the fits.

5.3 Dependence on the extent of the rotation curve

In Fig. 13, we show the average value of the ratio $\chi^2_{v_{ISO}}/\chi^2_{v_{NFW}}$ after truncating the 10-Mpc theoretical velocity profiles at different radii and repeating the fits. We quantify the extent of a curve by the number of points inside the truncation radius, N_{points}, which we vary from 10 to approximately 3.3 times the optical radius, roughly corresponding to 65 points in Dwarf1 and to 182 points in Dwarf4, the most extended galaxy in our sample. According to Fig. 13, V_{dm} is always better represented by the NFW formula independently of the truncation point. V_{tot} is also better represented by the NFW profile but still marginally consistent with the ISO model. In
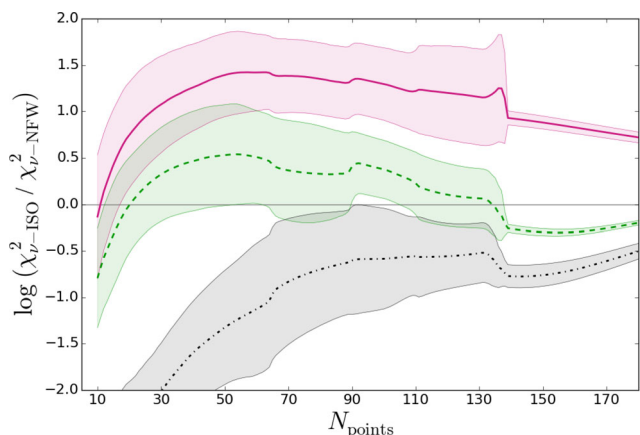
Figure 13. Dependence of the χ_ν^2 ratio on the extent of the rotation curves. N_{points} represents the number of points considered for the fit. The horizontal line represents equality between the models. We show the results for V_{dm} (magenta, solid line), V_{tot} (green, dashed line), and V_{cir} (black, dot–dashed line) for galaxies placed at 10 Mpc ($\sim$100 pc inner resolution). The reported lines denote the mean trends from all galaxies (or those reaching a given radial extent), whereas the shaded regions represent the 1σ scatter. Beyond 134 points the only contributor is D4, which is why the scatter is much smaller than at smaller radii. This plot demonstrates that the conclusion that V_{dm} and V_{tot} are better fit with the NFW model (in the sample as a whole), whereas V_{cir} (and the mock observed rotation curves, which are not shown) is better fit with the ISO model, is effectively independent of the truncation radius employed.

contrast, V_{cir} is better fit by the ISO profile for any truncation radius, although for small values of N_{points}, the difference between models is more extreme because the fake inner core dominates the fits. We do not plot equivalent profiles for the mock observations to avoid overcrowding the figure, but we note that they behave in the same manner as V_{cir}. Thus, the underestimation of the first points of the rotation curves determines the outcome of the rotation curve fitting analysis (i.e. the detection of spurious DM cores), regardless of the extent of the kinematic observations. Consequently, our specific choice to truncate the velocity profiles at approximately two times the optical radius does not affect the main conclusions of this work. At larger distances, we observe exactly the same qualitative results and the same shape for the $\chi_{\nu_{ISO}}^2/\chi_{\nu_{NFW}}^2$ radial profiles.

We remade the main plots presented in Section 4 but with the truncation radii of all the curves varying between $\sim$1 and $\sim$3 times the optical radius, and we observed only minor differences in the results. In particular, we noted that when using more extended rotation curves, the fits to V_{ls} less often preferred the ISO model than when the fiducial truncation radius was used. Once again, this is due to the fact that in the long-slit case, the Hα error bars are larger than the H I error bars, such that the effect of the inner core on the fit is progressively diminished as more outer points are used in the χ_ν^2 calculation.

5.4 Comparison with the literature

5.4.1 Comparison with observational results

In Fig. 14 (left), we present the coefficients (c, v_{200}) of the best NFW fit obtained for each velocity profile in our study, along with a collection of observational results from the literature based on high-resolution rotation curves. We fit our rotation curves trying all possible extents from one to three times the optical radius (typical of observations) in order to approximate the stochasticity of real

data. This is equivalent to maximum extents of between 2.6 and 29 kpc and N_{points} between 42 and 180, depending on the size of the galaxy.

We note that the coefficients c and v_{200} from the fits appear correlated both in our simulations and in the observational data and, more importantly, that our fits are very consistent with the parameter space spanned by observations. Strikingly, this is only true when our results consider different truncation radii and different distances together, as the fits to our fiducial mock data (truncated at two times the optical radius) at 10 Mpc cover just a narrow subset of the whole parameter space, roughly $\log(v_{200}) \leq 2$ and $\log(c) \geq 0.8$, as indicated with the shaded grey region in the plot. The agreement between observations and the fits to our mock data is enhanced by the inclusion of fits to less-extended versions of our rotation curves, probably because many observational studies use only Hα information, and they often do not reach the same radial extent as our fiducial mock data set. This is related to another facet of the cusp–core problem pointed out by observational studies, according to which the few reasonable NFW fits to real galaxies prefer large values of v_{200} and very low concentrations, which are not compatible with the mass–concentration relation predicted by cosmological simulations. As our results illustrate, this might originate in the large dependence of the observational analyses on subtle details and thus may not represent a genuine discrepancy between ΛCDM cosmological simulations and observations.

We repeat the same experiment with the ISO model and present the results and a comparison with the literature in Fig. 14 (right). The shaded region encloses the subset of the parameter space covered by the fits to galaxies at 10 Mpc using the fiducial extent of the rotation curves ($2 \times R_{opt}$). The full set of results includes fits to the mock rotation curves truncated at different radii, ranging from one to three times R_{opt}. Our fits populate a region of the ρ_o–R_c parameter space that is consistent with the observational works, although they do not fully cover the low ρ_o–high R_c end of the observed relation. This time the disagreement is only slightly alleviated by the use of different distances and truncation radii, i.e. despite the fact that the effects we discuss in this work offer a plausible explanation for the cusp–core discrepancy in terms of logarithmic density slopes, they are not sufficient to explain the largest cores inferred from ISO fits to real galaxies, associated with the large diversity of dwarf galaxy rotation curves, as discussed by Oman et al. (2015). It is also interesting to note that our fits naturally produce a correlation between ρ_o and R_c that agrees extremely well with that evident from observations. More specifically, both 'free' parameters lie on a straight line with a slope close to -1, which corresponds to a relation of inverse proportionality (the product $\rho_o \times R_c$ is approximately constant). This observation has been used to argue that DM haloes are cored and exhibit a constant inner surface density as some sort of universal property (see Spano et al. 2008; Kormendy & Freeman 2016, and references therein); however, the physical meaning of this conclusion is clearly put into question by our results.[5]

---

[5] Note that Spano et al. (2008) and Kormendy & Freeman (2016) did not use the pseudo-isothermal sphere model but a variant known as the nonsingular isothermal sphere, but Kormendy & Freeman (2016) found the core radius and the central surface density estimated from one model to be proportional to the corresponding quantities in the other model, so, our discussion regarding the alleged $\sim$constancy of $\rho_o \times R_c$ is straightforward.
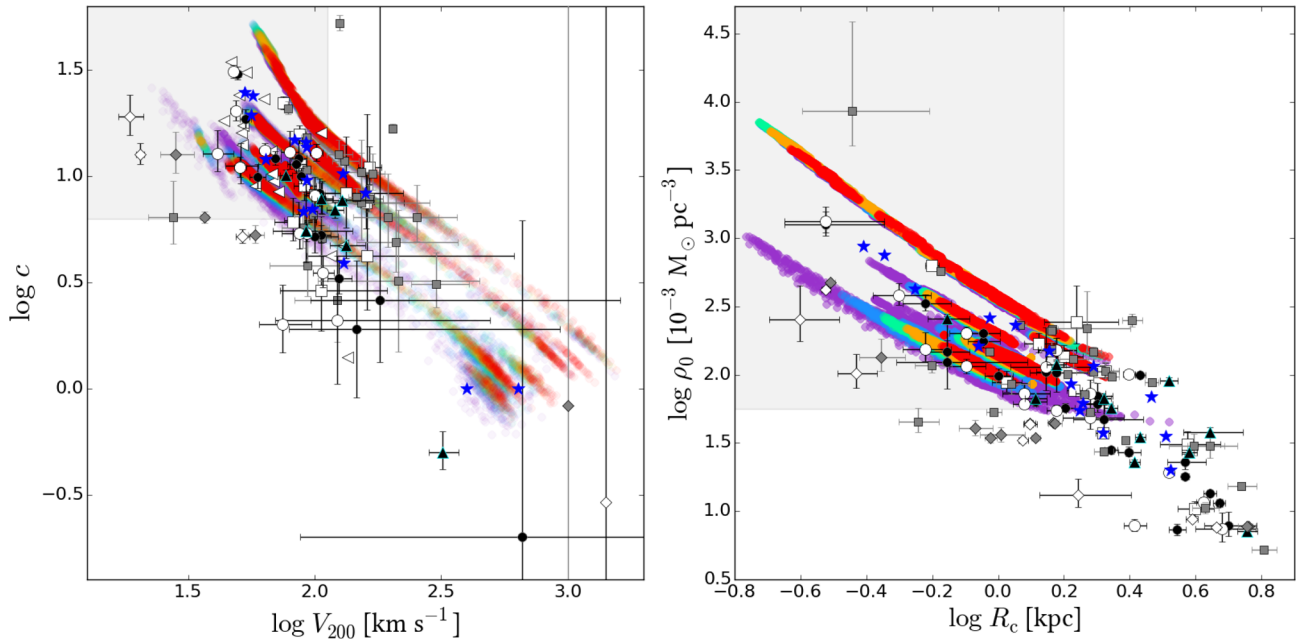
Figure 14. Coefficients of the best fits to our mock rotation curves (NFW models on the left, ISO models on the right) compared with observational results from the literature. We used different extents for the mock rotation curves, ranging from one to three times the optical radius. Results are colour-coded by inclination as in Fig. 8. The following background markers represent observational results from the literature: circles (de Blok & Bosma 2002), triangles (Kuzio de Naray et al. 2006), stars (Swaters et al. 2003), squares (de Blok et al. 2001), left-pointed triangles (van den Bosch & Swaters 2001), and diamonds (Oh et al. 2011a). White symbols represent fits for which the gas contribution was subtracted from the observed rotation curve before the fitting (but a mass-to-light ratio of zero was still assumed for the stellar component). We include error bars whenever they are reported. Note that de Blok et al. (2001), de Blok & Bosma (2002), and Oh et al. (2011a) estimated (c, v_{200}) in alternative ways for some galaxies when the best-fitting c value was negative or too close to zero; we do not include those galaxies in our comparisons. The positions of the simulated galaxies in the (c, v_{200}) plane depend on the distance to the galaxy and the radial extent of the mock data. At 10 Mpc, NFW fits to curves with fiducial extent $(2 \times R_{opt})$ lie in a subset of the parameter space spanned by observations, roughly $\log(v_{200}) \leq 2$ and $\log(c) \geq 0.8$, as indicated with the grey square in the plot. Only when a larger diversity of extents and distances is allowed we see the NFW fits almost covering the full parameter space that observations do. A similar trend occurs for the ISO model, though it appears less dramatic. At 10 Mpc, fits to curves with the fiducial extent lie on the shaded grey region, and slightly larger, less-dense cores are only recovered when we try different extents and distances. Nevertheless, none of the fits to our mock data is able to reproduce the largest, least dense cores observed in some galaxies. Interestingly, as the ISO fits to our simulated data represent illusory cores, and they reproduce the correlation between ρ_o and R_c that has been obtained for real galaxies, this may be an artefact of the fitting process rather than a physical relation obeyed by real DM haloes.

5.4.2 Comparison with simulation works employing similar methodologies

We now put our work into context by means of a brief comparison with other studies that have investigated how well the inner shape of DM profiles can be extracted from synthetic observations of simulated galaxies.[6] We start with the pioneering work of Rhee et al. (2004), which found that bars, small bulges, and projection effects induce underestimates of the inner circular velocities that can prevent the detection of cuspy DM haloes, making them look cored. The authors mention that the individual effects lead to velocity errors of only a few km s^{-1}, but their cumulative effect can result in qualitatively incorrect conclusions.

This result is consistent with our study, but we note that the reason for this agreement is not straightforward because Rhee et al. (2004) did not simulate the gaseous phase. The velocity underestimation they observe is partially due to the dynamics of the stellar component (the so-called asymmetric drift effect, see Section 5.5.1) and to projection effects. Fig. 19 of Rhee et al. (2004) suggests that

---

[6] Here, we refer to *N*-body numerical simulations, not to synthetic observations generated via analytic models. The advantage of the former is that they are more suitable for studying the 3D dynamical evolution of galactic systems in a self-consistent way.

in axisymmetric systems, the inferred DM density profile slightly flattens, although it does not present a strong core. In contrast, in the presence of small bulges and bars, the combination of the former effects and non-circular motions makes the inferred density profiles artificially cored.

Interestingly, Rhee et al. (2004) show with convincing observational evidence that stars and ionized gas rotate similarly in the inner region, contrary to the general belief that the gas rotates faster because it is a dynamically colder component. The authors list possible explanations for this behaviour that have been suggested in the literature, including pressure support. In our simulations, the rotational velocities of the stellar and the gaseous particles inside the first kiloparsec are indeed similar, but not identical. In general, we find the gaseous rotation curves to be more lowered in the very centre, whereas beyond ~ 0.5–1 kpc, the stellar component rotates more slowly. This means that the matter distribution recovered from the gaseous V_{cir} will tend to be flatter, explaining why we infer the presence of spurious cores even in systems without bulges or bars.

Valenzuela et al. (2007) further investigated the impact of systematic effects and presented detailed mass modelling of the dwarf galaxies NGC 3109 and NGC 6822. They compared collisionless *N*-body simulations and full hydrodynamical runs with and without star formation and stellar feedback and found that without feedback, the gas rotational speed is similar to the true circular velocity

of the gravitational potential. In contrast, once injection of thermal energy from stellar processes into the ISM is included, the gaseous phase rotates considerably more slowly as a result of pressure support. This effect creates a notable flattening of the inferred density profile, which is further accentuated by the presence of a small bar and projection effects. Valenzuela et al. (2007) clearly illustrated how non-circular motions related to small asymmetries in the baryonic matter distribution, which might be easily overlooked, can bias the measured rotational velocities towards core-like profiles. An exhaustive analysis of asymmetric drift and pressure support corrections is also presented; Valenzuela et al. (2007) conclude that it is possible to recover the true circular velocity from the observed gaseous rotation curve in their models, but this requires very careful, detailed corrections for numerous systematic effects, even for axisymmetric discs. They also emphasize that observing low-rms velocity dispersions ($\sim$10 km s^{-1}) in a galaxy does not mean that such corrections can be safely neglected. Overall, we find our results to be in very good agreement with those of Valenzuela et al. (2007) and Rhee et al. (2004).

Kuzio de Naray & Kaufmann (2011) analysed mock observations of simulated galaxies embedded in cuspy, cored, and triaxial DM haloes. They generated realistic mock observations by choosing the spatial resolution, spatial coverage, and inclination according to the observational sample studied in Kuzio de Naray et al. (2006) and Kuzio de Naray et al. (2008). Kuzio de Naray & Kaufmann (2011) found that typical rotation curve analyses are able to efficiently recognize the cuspiness of a DM halo and that it should be possible to observe the characteristic signature of a DM cusp in velocity maps. Particularly, in cored spherical haloes, the iso-velocity contours appear parallel in the centre of the galaxy, whereas in spherically symmetric cuspy DM haloes, the central velocity contours are 'pinched'. The authors present examples of mock velocity fields in which such features are evident. They also found that stellar feedback had little effect on the mock velocity fields and observed rotation curves.

Why these results are so different from those referenced earlier is difficult to understand, especially noting that Kuzio de Naray & Kaufmann (2011) used the same code as Valenzuela et al. (2007). In the latter, stellar feedback was proven to be an efficient source of pressure support; thus, we speculate that the specific feedback implementation might have been different in Kuzio de Naray & Kaufmann (2011), leading to weaker pressurization of the ISM. Alternatively, the simulations of Kuzio de Naray & Kaufmann (2011), which were initially composed only of gas and DM, might not have formed a sufficient number of stars for stellar feedback to pressurize the ISM significantly. We highlight the fact that using a different code with an independent stellar feedback implementation, our own simulations, which represent real galaxy populations in terms of the amount of gas and stars in the disc, reproduce the previous findings of Valenzuela et al. (2007) regarding the role of pressure support. We also note that our velocity fields are not pinched in the centre; instead the iso-velocity contours appear parallel there (see Fig. 3).

Oh et al. (2011b) analysed mock velocity fields and images of two dwarf galaxies formed in cosmological simulations in the same manner as a sample of dwarfs previously studied in Oh et al. (2011a). The authors did not use the minimum disc approximation but rather attempted to subtract the contributions of gas and stars from the mock rotation curve. They were able to approximately recover the true DM density distribution from the mock observations using typical tilted-ring modelling, and they state that pressure support effects and non-circular motions did not hamper this recovery. Nevertheless, one of their two recovered DM density profiles underestimated

the true density by a factor of 3 in the central region, but they associated this to errors in the estimation of the gravitational potential of the gas. Oh et al. (2011b) found good agreement between their simulation results and observations. They concluded that DM cores likely exist in the sample of real galaxies and that the mechanisms which transform DM cusps into cores in their cosmological simulations (i.e. violent outflows of gas caused by repetitive, intense starburst episodes) are plausible. However, an important cautionary note is that Oh et al. (2011b) only analysed mock observables when the DM haloes were already cored; therefore, this work does not lend insight into the possibility of identifying DM cusps via the same type of analysis. Regardless of whether it is possible to infer the presence of cores via rotation curve fitting, our results (and others mentioned above) suggest that cusps may be mistaken for cores and thus the cusp–core problem may be an illusion.

5.5 Can pressure support effects be corrected?

Now that we have demonstrated the crucial role of pressure support in cusp–core studies, we address the matter of whether its effect may be corrected using observationally accessible information.

5.5.1 Pressure support versus asymmetric drift

First, we would like to clarify the theoretical concepts related to the physics of pressure support, as there is some ambiguity in the literature. Our main concern is the use of the terms pressure support and asymmetric drift as interchangeable expressions despite the fact that they represent different physical properties. This common mix-up was recently pointed out by Dalcanton & Stilp (2010), but it still deserves further attention, as we will demonstrate below.

One can start by stating what pressure support truly means and its proper formulation. Consider the Euler momentum conservation equation for a gas element in an external gravitational field,

$$\frac{\mathrm{d}\boldsymbol{V}}{\mathrm{d}t} = \boldsymbol{a}_{\mathrm{grav}} - \frac{1}{\rho}\nabla P. \tag{24}$$

If this gas element moves on a circular orbit in the mid-plane of a system with axial and vertical symmetries, the three terms of equation (24) are aligned in the radial direction, leading to the scalar relation

$$\frac{v_\phi^2}{r} = \frac{v_c^2}{r} + \frac{1}{\rho}\frac{\mathrm{d}P}{\mathrm{d}r}, \tag{25}$$

where v_ϕ represents the rotational speed of the gas; v_c is the expected circular velocity from the gravitational potential; and the second term on the right is the radial acceleration due to pressure gradients, ρ being the gas density, and P its pressure. The sign inversion on the right-hand side is because centripetal accelerations point inwards, i.e. in the negative $\boldsymbol{r}$ direction. Note that if pressure falls off as a function of radius (as it is often the case in galactic discs), the gradient becomes negative, making $v_\phi < v_c$; this is pressure support. Also note that equation (25) is valid in the equatorial plane for any combination of spherical and disc-like components, so the approximation of a spherical potential ($a_{r_{\mathrm{grav}}} \approx \frac{GM(<r)}{r^2}$) used by Dalcanton & Stilp (2010) is not necessary.

The sources of pressure typically mentioned (if any) in the cusp–core literature are thermal pressure and turbulence. Other possible sources, such as magnetic fields or cosmic rays, are rarely mentioned, although they may be important for the dynamics of the ISM (Boulares & Cox 1990; Ferrière 2001; but cf. Su et al. 2016). Dalcanton & Stilp (2010) highlight that turbulence dominates the

random motions of the gas and for that reason the pressure relates to the 1D velocity dispersion as

$$P = \rho \sigma^2. \tag{26}$$

Substituting equation (26) into equation (25), rearranging terms, and expressing the velocities in our notation, the pressure support correction can be written as

$$V_{\mathrm{tot}}^2 = V_{\mathrm{cir}}^2 - \sigma^2 \frac{\mathrm{d} \log \left(\rho \sigma^2 \right)}{\mathrm{d} \log r}. \tag{27}$$

Furthermore, assuming that the vertical structure of the disc does not depend on radius, one can express the logarithmic derivative in terms of the mass surface density of the gas Σ, which is the observable quantity

$$V_{\mathrm{tot}}^2 = V_{\mathrm{cir}}^2 - \sigma^2 \frac{\mathrm{d} \log \left(\Sigma \sigma^2 \right)}{\mathrm{d} \log r}. \tag{28}$$

This is equivalent to equation 11 of Dalcanton & Stilp (2010). We have omitted the subindex r in the velocity dispersion to emphasize that turbulence is classically treated as an isotropic source of pressure.[7] Dalcanton & Stilp (2010) argue that the distinctive boundary conditions in the vertical direction and in the equatorial plane likely invalidate the assumption of isotropy in the velocity dispersion, which is indeed a relevant concern for the macroscopic scales probed by observations. Nevertheless, in practice, σ is in general treated as isotropic, mostly due to the difficulty of disentangling its radial component from the observed projection along the line of sight.

Asymmetric drift, on the other hand, is a phenomenon experienced by collisionless particles. Its origin is succinctly presented in Binney & Tremaine (2008), to which we refer the reader for details. In brief, the Jeans equations for a stellar population rotating in the equatorial plane of a smooth potential with axial and vertical symmetries yield

$$v_{\mathrm{c}}^2 - \overline{v_\phi}^2 = \sigma_\phi^2 - \overline{v_r^2} - \frac{r}{\nu} \frac{\partial (\nu \overline{v_r^2})}{\partial r} - r \frac{\partial (\overline{v_r v_z})}{\partial z}, \tag{29}$$

where v_{c} represents the circular velocity associated with the gravitational potential, v_r, v_ϕ, and v_z are the three components of the actual stellar velocity, σ_ϕ is the azimuthal velocity dispersion, and ν is the probability of finding a star at a certain position. The last quantity is proportional to the mass density of the tracers and can be replaced by the mass surface density Σ if the vertical structure of the stellar distribution does not vary with radius. Assuming no net radial motions ($\overline{v_r^2} = \sigma_r^2$) and using our notation, equation (29) becomes

$$V_{\mathrm{tot}}^2 = V_{\mathrm{cir}}^2 + \sigma_\phi^2 - \sigma_r^2 - \sigma_r^2 \frac{\mathrm{d} \log (\Sigma \sigma_r^2)}{\mathrm{d} \log r} - r \frac{\partial (\overline{v_r v_z})}{\partial z}. \tag{30}$$

The similarity of equations (30) and (28) is remarkable, but further assumptions are needed if one wants to make them look identical. These are (1) that there are no tilts in the velocity ellipsoid, so the last term of equation (30) vanishes, and (2) that the velocity dispersion of the stars is isotropic. Neither of these assumptions is straightforward, so, in spite of the fact that the Euler and the Jeans equations can be obtained from the Boltzmann equation in similar fashions, they are not physically equivalent.

---

[7] This seems to be a good approximation when the dominant contribution comes from microturbulence at much smaller scales than the size of the region being considered (Mac Low & Klessen 2004; but cf. Elmegreen & Scalo 2004).

Some authors explicitly suggest that ionized gas might actually experience the effects of asymmetric drift if it is clustered into individual clouds which dynamically behave like collisionless particles (e.g. Cinzano et al. 1999; Verdoes Kleijn et al. 2000; Weijmans et al. 2008). Invariably, all the studies addressing this hypothesis are focused on early-type galaxies which are dynamically hot, exhibiting internal velocity dispersions of hundreds of km s^{-1} that are hard to reconcile with thermal agitation and small-scale turbulence. On the other hand, late-type galaxies such as those regularly studied in the cusp–core literature are comparatively cold systems, with reported H I velocity dispersions of the order of $\sim$12 km s^{-1}. These small velocity dispersions can be naturally explained by thermal and turbulent pressures. Therefore, there is no need to invoke alternative scenarios. Note also that a large fraction of the 21-cm emission comes from the warm (6000–10 000°K) neutral gas in the disc, which, in contrast with the clumpy, cold (100°K) H I phase, is a diffuse medium with a large spatial extent (Ferrière 2001). The same applies for the warm ($\sim$8000°K) ionized medium responsible for the diffuse Hα emission outside of H II regions (Cox 2005). In light of these facts, it seems more likely that the dominant source of non-centrifugal support in gaseous discs of late-type galaxies is pressure support, not asymmetric drift. Incidentally, we note that equation (28), which describes pressure support, is the universal recipe employed to correct gaseous rotation curves affected by random motions in cusp–core studies, but it is often improperly named 'the asymmetric drift correction'. Sometimes equation (30) is invoked, but then the precise supplementary approximations to reduce it to equation (28) are invariably assumed.

The trouble with conflating pressure support and asymmetric drift is that this may lead to an erroneous assessment of the magnitude of the correction. Note that in equation (30), all the quantities refer exclusively to the stellar population that is being traced, while in equation (28), they refer to the gaseous medium as a whole. One may argue that according to the classic pictures of the ISM (Field, Goldsmith & Habing 1969; McKee & Ostriker 1977), the different phases are expected to coexist in thermal pressure equilibrium; if so, tracing a single phase (for instance, the warm H I) provides information about the global thermal state of the ISM. Nevertheless, this scenario is an oversimplification, and thermal pressure imbalances have been observed even in the local ISM (Bowyer et al. 1995; Berghöfer et al. 1998). This implies either that pressure equilibrium must include non-thermal sources that are dynamically important, such as turbulence, magnetic fields, and cosmic rays (Ferrière 2001; Cox 2005), or that pressure imbalances may exist locally as a result of complex events such as recent supernova explosions, for instance. Therefore, a comprehensive assessment of the dynamical state of the gas through multiple observational tracers is highly desirable.

Some authors have expressed concerns about the estimation of the gas velocity dispersion and the gas surface density profiles from a single tracer, as this may bias the measurements in regions with significant fractions of other ISM components (e.g. Simon et al. 2003; Dalcanton & Stilp 2010). Regrettably, these biases are most often simply overlooked, and the majority of the cusp–core literature considering pressure support only vaguely states that random motions may provide support to the gas when they are comparable to the rotation velocity. A fraction of this subset of studies argues that pressure support corrections are known to be unimportant, increasing the magnitudes of rotation curves by only a few km s^{-1}, and do not attempt any sort of correction. The remaining fraction applies equation (28) to the data at hand, normally from only a single tracer, often without considering the uncertainties in this correction. As we will demonstrate below, effective corrections
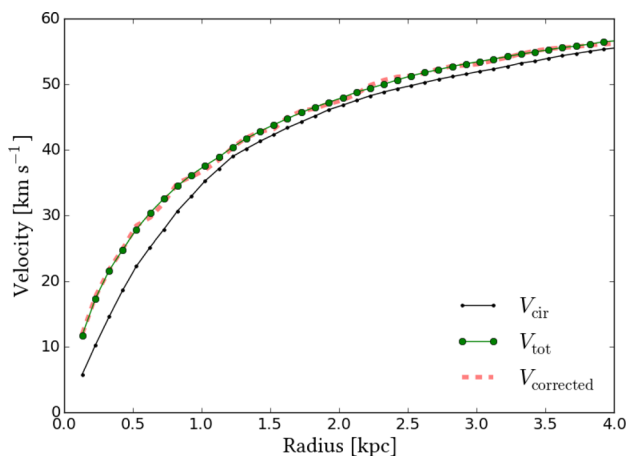
Figure 15. Theoretical verification of the pressure support effect in galaxy Dwarf1 at half the simulation time. The solid green line with circles represents V_{tot}, the black solid line with points represents V_{cir}, and the long-dashed red thick line in the background is the corrected version of V_{cir} after adding the term on the right-hand side of equation (27). The correction exactly recovers V_{tot} from V_{cir}, confirming pressure support as the cause of their difference.

for pressure support effects may be much more challenging than has been traditionally assumed.

5.5.2 Ideal and realistic pressure support corrections

We here study the feasibility of pressure support corrections in our models, first based on ideal theoretical measurements and then using observationally accessible information, i.e. the surface density profiles (Σ) and the velocity dispersion profiles (σ), obtained from the corresponding mock maps by taking azimuthal averages along the same elliptical rings used to analyse the velocity maps.

We start by checking the validity of equation (27) directly in the simulations. We measure σ and ρ from all gas particles in the equatorial plane using the same radial bins as for the theoretical velocity profiles. The velocity dispersion is calculated using equation (13), recalling that the code indirectly models the effect of the turbulence induced by stellar and supernova feedback by employing an effective equation of state that is stiffer than isothermal, thereby enhancing the pressure and thus temperature in high-density, star-forming gas. By means of equation (27), we find exceptional agreement between V_{tot} and the corrected version of V_{cir} for all galaxies, as we illustrate with an example in Fig. 15. Moreover, the results of the NFW/ISO fits to the corrected version of V_{cir} are in stunning agreement with those of V_{tot}, as we report in Table 5. The correction is performed using the theoretical profiles in radial bins of 100-pc width. The fits reported at distances $D = 20$ Mpc in Table 5 are done after resampling the corrected curves to the corresponding poorer spatial resolution.

Notwithstanding, even though the pressure corrections work properly in the ideal case, a number of difficulties prevent effective correction of the mock observations. After applying equation (28) to our mock rotation curves using the *observed* Σ, σ profiles, the cuspy DM haloes still appear disguised as cores to the rotation curve fitting method, as we also show in Table 5. To understand this result, we need to discuss in detail several aspects of the implementation of equation (28).

The first difficulty in correcting for pressure support based on observed quantities is that virtually all the cusp–core studies con-

Table 5. Percentages of corrected rotation curves that are better represented by the NFW or ISO models. For comparison, we include the results from V_{tot}, which were already presented in Table 2. We do not correct the mock observations at 40 or 80 Mpc because the H I spatial resolution is too low.

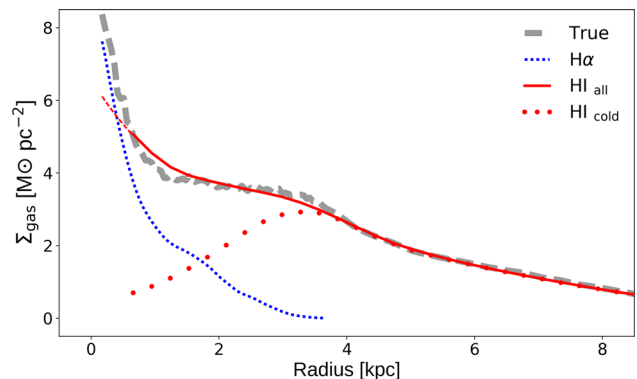| Hα PSF (pc)		$\sim$100	$\sim$200
D (Mpc)		10	20
V_{tot}	NFW	56 (61)	57 (61)
	ISO	38 (39)	39 (39)
	Both	6 (0)	4 (0)
V_{cir} (corrected)	NFW	57 (61)	58 (60)
	ISO	37 (39)	36 (38)
	Both	6 (0)	6 (2)
V_{kin} (corrected)	NFW	15 (21)	13 (20)
	ISO	67 (74)	69 (77)
	Both	18 (5)	17 (4)

Figure 16. Gas surface density profiles for G0 at 3 Gyr, 45° inclination, and a distance of 10 Mpc. The thick dashed grey line represents the true mass surface density profile as measured from the simulation. The dotted blue line is the Hα surface brightness profile, re-scaled to have a central amplitude similar to that of the true mass profile. The solid red line shows our fiducial $\Sigma_{H I}$ mass surface density profile, extrapolated in the very centre with an analytical function represented by a thin dashed line. The red dots represent the alternative observation from the cold gas alone, $\Sigma_{H I\text{-}cold}$. The low spatial resolution smoothes the $\Sigma_{H I}$ profile and leads to an underestimation of the central gas concentration. Observations from the cold H I phase would be more strongly biased in the centre, where most of the gas in our simulations is hot and forming stars.

sidering this effect use H I data alone, with very few exceptions that use kinematic data from the ionized gas but then lack the H I extension (Simon et al. 2003; Chemin et al. 2016). Extrapolating a sort of 'standard' observational correction for our case, we correct the inner Hα velocities using the $\sigma_{H\alpha}$ velocity dispersion and the outer H I velocities using $\sigma_{H I}$. For the gas surface density profile, we take $\Sigma_{H I}$ at all radii. Because the H I spatial resolution is coarser than that of the Hα observations, it is necessary to extrapolate the $\Sigma_{H I}$ profile in the centre. We achieve this by fitting a polynomial-plus-Gaussian function to the first 10 kpc of $\Sigma_{H I}$, checking that it follows the data well and that it exhibits reasonable asymptotic behaviour in the inner region. Then, we calculate the pressure support correction at each point of the rotation curves by evaluating the derivatives in equation (28) with a finite-difference scheme. In Figs 16 and 17, we present an example of the mass surface density profile and of the velocity dispersion profile as traced by different gas phases, along
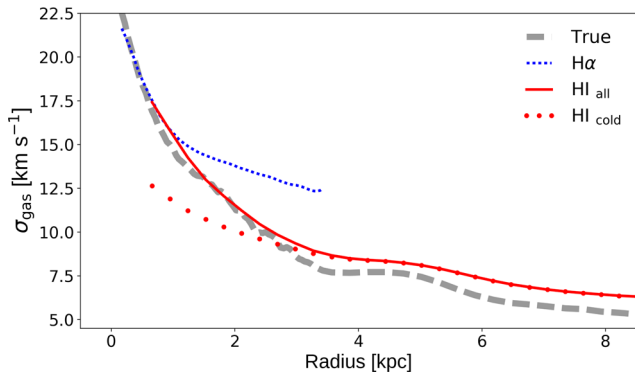
Figure 17. Velocity dispersion profiles for G0 at 3 Gyr, 45° inclination, and a distance of 10 Mpc. Colours and symbols are the same as in Fig. 16, identifying the true profile in the simulation and those inferred from our mock Hα, H I, and H I$_{cold}$ observations. This plot shows that in areas where hot and cold gas coexist, measurements based on a single tracer differ from the true values.

with the true quantities from all the gas in the equatorial plane of the simulations. Because our mock H I observations use all the gas particles regardless of their physical state, we also show for comparison the profiles extracted from the cold gas ($T < 10^4$ °K) alone, which may be a better proxy for real H I observations. We note that unlike the H I case, our mock Hα emission is not only proportional to the mass but also the SFR of the emitting particles, making the conversion factor between the intensity maps and the gaseous mass uncertain. For this reason, we plot the mock Hα luminosity profile in Fig. 16, rescaled as necessary to facilitate the comparison with the surface mass density profiles. These plots are for a specific observed galaxy, but similar trends are observed for the rest of the sample.

Recalling that our mock Hα emission traces only the star-forming gas, a joint analysis of Figs 16 and 17 reveals that there are three different regimes in the disc. In the very inner region, within ~0.6 kpc, virtually all of the gas is forming stars, and both the $\Sigma_{H\alpha}$ and $\sigma_{H\alpha}$ profiles follow well the true theoretical quantities. At intermediate radii (between ~0.6 and ~3.5 kpc), there is a mix of star-forming and non-star-forming gas, with the Hα emission steeply going to zero while the cold gas density steadily grows. Taking into account that the star-forming gas is systematically hotter than average, this explains why in this intermediate regime, $\sigma_{H\alpha}$ increasingly overestimates the true global velocity dispersion, while $\sigma_{H I-COLD}$ stays below the true σ profile but systematically approaches it as the fraction of cold, non-star-forming gas starts to dominate. We also note that in this intermediate region, the slope of $\sigma_{H\alpha}$, which will influence the pressure correction term, is shallower than that of the true total velocity dispersion profile. Beyond ~3.5 kpc, virtually all the gas in the simulation is cold and passive, there is no mock Hα emission and the measurements from the cold gas phase coincide with our fiducial H I observations. In general the fiducial mock H I observations follow the true theoretical quantities well, though the low resolution makes the observed profiles appear smoother and σ slightly overestimated. This smoothing propagates and introduces a bias during the extrapolation of $\Sigma_{H I}$ to the very centre, leading to an underestimation of the true total surface density and also of its steepness.

We have shown that there are biases in both the amplitude and the slope of the observationally inferred Σ and σ profiles at different radial ranges and from different tracers. Regarding posterior cusp–core analyses, in which direction will these biases act? The answer
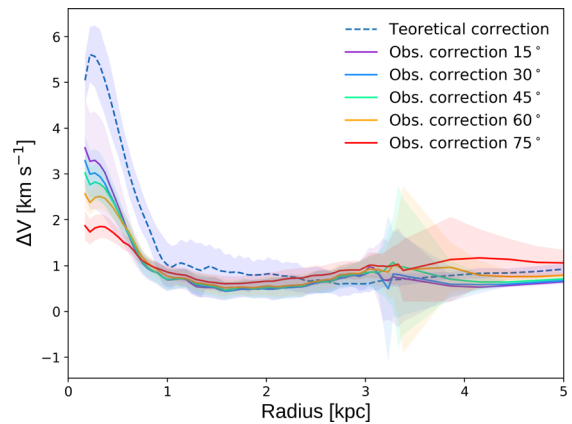

Figure 18. Theoretical and observational pressure support corrections for galaxy Dwarf2 viewed at 10 Mpc. We plot the net velocity excess Δv to be added to the observed rotation curves (or to V_{cir}) to get their corrected versions. Solid lines represent the mean correction as a function of radius, and the shaded regions enclose the 1σ scatter of the profiles. The observational corrections are colour-coded by inclination as indicated in the legend. This plot shows that observational corrections underestimate the theoretical correction as a result of biased estimates for Σ and σ; even though the difference seems small, it prevents faithful recovery of the inner curvature of the observed rotation curves, which still appear more compatible with the ISO model after the attempted correction.

depends largely on the logarithmic slope of the product $\Sigma \sigma^2$, i.e. on its curvature, which cannot be simply inferred from our qualitative analysis. After evaluating equations (27) and (28) we found that, for our particular experiment and for the choices we made, the observational correction exhibits the right radial profile but it falls behind the theoretical expected value. We show this in Fig. 18, where we present the net difference between the corrected velocity profiles and the original ones, Δv, as a function of radius and inclination. The mean difference between the theoretical and the observational corrections is never larger than 4 km s^{-1}, falling between 1 and 2 km s^{-1} over most of the first kiloparsec. However, this small difference is enough for the intended observational correction to fail because the curvature of the 'corrected' rotation curves is still more compatible with the ISO model in at least 67 per cent of the sample (see Table 5). In spite of the fact that the tension is slightly less critical than before the correction, the inferences from the rotation curve fitting continue to be misleading compared with those from V_{tot}, largely overestimating the fraction of 'observed' cores because of the inaccurate pressure support corrections.

Fig. 18 and Table 6 also demonstrate that the magnitude of the pressure support is more underestimated, i.e. the correction is less effective, in more inclined discs. This is as a result of projection effects and the low spatial resolution, which make the Σ and σ profiles flatter, thus lowering the inferred logarithmic slope of the product $\Sigma \sigma^2$. We do not correct the mock observations at 40 or 80 Mpc because the observables are extremely biased by the effect of the spatial resolution. Particularly, note that at 40 Mpc, the first $\Sigma_{H I}$ data point lies at 2.4 kpc, ruling out any possibility of performing an accurate correction inside the first kiloparsec.

It is very interesting to note that the observationally inferred Δv values peak at ~3.5 km s^{-1} and quickly drop to ~1 km s^{-1}, in agreement with typical corrections estimated from observations, which are sometimes interpreted as a reflection of the insignificant role of pressure support. This conviction is often supported by the observed low velocity dispersions, typically ~10 km s^{-1}. However, note

Table 6. Percentages of rotation curves extracted from the 2D maps that are better represented by the NFW or ISO models after the observational pressure support corrections.

Hα PSF (pc)		∼100	∼200
D (Mpc)		10	20
15°	NFW	22 (31)	19 (28)
	ISO	55 (63)	57 (66)
	Both	22 (6)	24 (6)
30°	NFW	24 (31)	20 (28)
	ISO	57 (64)	61 (69)
	Both	19 (5)	19 (3)
45°	NFW	19 (26)	17 (24)
	ISO	61 (70)	63 (71)
	Both	20 (4)	20 (5)
60°	NFW	8 (15)	8 (14)
	ISO	70 (78)	74 (82)
	Both	22 (7)	18 (4)
75°	NFW	1 (3)	0 (0)
	ISO	93 (96)	98 (99)
	Both	6 (1)	2 (1)

that this estimate regularly comes from H I data alone, and that in general, the ionized gas is expected to have a larger velocity dispersion, one of the reasons why it tends to form thicker discs than the neutral gas (Fathi et al. 2007). Fig 17 reveals that the cold dynamical component in our simulations looks similar to many H I observations in this regard, peaking at ∼13 km s^{-1} and exhibiting a smooth radial gradient; however, we know that this tracer is extremely biased relative to the full velocity dispersion of the whole gas, which is the necessary quantity for accurate pressure support corrections.[8] The true value of σ in our simulations peaks at ∼25 km s^{-1} and steeply decreases, dropping to ∼10 km s^{-1} at ∼2 kpc. This is compatible with the few reported Hα observations we could find in cusp–core works. For example, Simon et al. (2003) observed a line width of 34 km s^{-1} for the dwarf spiral NGC 2976, Epinat et al. (2010) mentions an average velocity dispersion of 24 km s^{-1} for a local sample of 153 nearby disc galaxies of mixed morphological types extracted from the Gassendi H α survey of SPirals (GHASP; Epinat et al. 2008a; Epinat, Amram & Marcelin 2008b), and Chemin et al. (2016) found a velocity dispersion profile peaking at 25 km s^{-1} and dropping to ∼20 km s^{-1} at 2 kpc for the grand-design spiral M99.

Note also that according to Fig. 16, the cold gas strongly underestimates the true gas density in the centre. Moreover, the inferred $\Sigma_{\text{H I-cold}}$ profile has a positive slope there, which would partially reverse the sign of the pressure support correction term if it were inserted in equation (28). Even though this modelling may be too simplistic to explain the complexity of real H I observations, it is interesting to note that central 'holes' in the $\Sigma_{\text{H I}}$ profiles are not rare, and they are treated in different ways when performing pressure support corrections; some authors use $\Sigma_{\text{H I}}$ as is, while others extrapolate the external exponential disc behaviour to the centre to try to compensate for the ionized and molecular hydrogen mass contributions, which are very difficult to assess.

It is not absolutely clear if the gas in our simulations may be overpressurized compared with real systems, but we consider that

---

[8] Interestingly, at inclinations ≤30°, the $\sigma_{\text{H I−COLD}}$ profile is even flatter and stays below 10 km s^{-1}.

the very good agreement between our mock data and real observations, as well as the agreement in the best-fitting coefficients presented in Fig. 14, should motivate further scientific discussion and careful review of some observational results. Independent of the possible differences between our models and real dwarf irregulars and LSBs, the exercise performed here suffices to demonstrate the intrinsic difficulties in properly assessing the effect of pressure support (amongst others), and it underlines the sensitivity of rotation curve fitting methods to very small errors or biases in the central parts of galaxies.

6 CONCLUSIONS

Our results demonstrate that pressure support effects can easily make DM cusps appear as cores in kinematic observations. Small errors of ∼5 km s^{-1} within the central kiloparsec are sufficient to completely remove the signature of a DM cusp if they coherently decrease the measured velocity. Thus, not correcting for pressure support can be catastrophic in the cusp–core context, even for high-resolution data generated from perfectly symmetric rotating discs. We highlight the fragility of this type of rotation curve analysis: small errors can lead to qualitatively incorrect conclusions regarding the shape of the inner DM profile. Because multiple sources of errors (e.g. beam-smearing, non-circular motions, small bulges, and projection effects) act in a similar manner as pressure support (i.e. they tend to cause the observed circular velocity to underestimate the true circular velocity in the center), even if the amount of pressure support present in our simulations differs in detail from reality, our main conclusion would still hold.

Strikingly, increasing the spatial resolution does not lead to more reliable conclusions. Instead, the ISO model is preferred more often when the simulated galaxies are placed at smaller distances because the signature of the fake core is better sampled. We also note that the coefficients of the best-fitting NFW profile strongly depend on the spatial extent of the rotation curve. Best fits to data that do not extend into the flat part of the rotation curve (which is often the case for Hα-only data) tend to prefer larger v_{200} values and lower concentrations. Our data are very consistent with the literature once we account for the different rotation curve truncation radii employed; this agreement pre-empts criticism regarding possible inconsistency between the coefficients of the NFW fits of real galaxies and the ΛCDM mass–concentration relation predicted by the *N*-body simulations.

Our best ISO fits also lie in the region of parameter space spanned by the results of observational studies and naturally reproduce the observed inverse proportionality between ρ_o and R_c. This result suggests that this correlation may be an artefact of the fitting process rather than a real physical property of DM haloes. It is interesting to note that beam smearing can dramatically impact Hα rotation curves of galaxies at ∼80 Mpc. This is not a surprise because linear resolution depends not only on the angular resolution but also on the distance at which a galaxy is located. None the less, this result must be emphasized because the high angular resolution of optical data is often interpreted as providing sufficient protection against beam smearing. This is evidenced by the large amount of galaxies more distant than 50 and even 100 Mpc that have been employed in some cusp–core studies. Projection effects also play an important role, making false detections of cores more likely in galaxies at high inclinations, especially at larger distances.

Our model galaxies do not support the widely accepted claim that the minimum disc approximation yields an upper limit on the true steepness of a DM halo density profile. In all our galaxies,

whose properties are carefully modelled after observations of real dwarf galaxies in the local Universe, the addition of baryons to the gravitational potential of the DM haloes makes the true circular velocity profiles flatter rather than cuspier. Thus, the minimum disc approximation would cause one to infer that the DM profile is flatter than it actually is.

As noted above, not correcting for pressure support can result in erroneous conclusions regarding the inner DM profile shape. After carefully defining pressure support and distinguishing it from asymmetric drift, we have examined whether it is possible to correct for pressure support using observables generated from our simulations. We find that even with the data available from the highest quality cusp–core studies, it is extremely challenging – if not impossible – to fully correct for pressure support, and, as noted above, even small errors of a few km s^{-1} can cause DM cusps to be disguised as cores.

The analysis presented here has highlighted the difficulties involved in reliably inferring the central DM structure in a rotation curve analysis of observational data. In particular, we have shown that it is comparatively easy to mistake a DM cusp for a DM core, even with high-quality data. This certainly suggests that previous observational claims of core detections need to be taken with a grain of salt and should be followed-up further.

Our simulations have limitations, of course, the most important ones being that they are idealized compound galaxy models that lack a self-consistent cosmological context and that they do not include explicit supernova 'blast wave' feedback, which some simulations have suggested can transform cusps into cores. It would thus be interesting to repeat a similar analysis with galaxies extracted from full cosmological hydrodynamic simulations of galaxy formation, which now have sufficiently high resolution to study the cusp–core problem (e.g. Hopkins et al. 2014; Marinacci et al. 2014; Vogelsberger et al. 2014b; Chan et al. 2015; Oñorbe et al. 2015; Schaye et al. 2015; Sawala et al. 2016). Such models could then also account for perturbations in the circular motions of the gas due to central black holes, galaxy encounters, and cosmological torques. However, we stress that the idealized nature of our simulations (which contain strong, unperturbed NFW cusps by construction and, with the exception of G1, are highly axisymmetric) should make it easier to detect cusps than would be the case if fully cosmological simulations with explicit stellar feedback were employed. For this reason, in reality, it may actually be more difficult to observationally identify cusps via rotation curve fitting than suggested by our work.

ACKNOWLEDGEMENTS

REFERENCES

Adams J. J. et al., 2014, ApJ, 789, 63
Agertz O. et al., 2007, MNRAS, 380, 963

Angulo R. E., Springel V., White S. D. M., Jenkins A., Baugh C. M., Frenk C. S., 2012, MNRAS, 426, 2046
Begum A., Chengalur J. N., Karachentsev I. D., Sharina M. E., Kaisin S. S., 2008, MNRAS, 386, 1667
Bell E. F., de Jong R. S., 2001, ApJ, 550, 212
Berghöfer T. W., Bowyer S., Lieu R., Knude J., 1998, ApJ, 500, 838
Bershady M. A., Verheijen M. A. W., Swaters R. A., Andersen D. R., Westfall K. B., Martinsson T., 2010, ApJ, 716, 198
Binney J., Tremaine S., 2008, Galactic Dynamics, 2nd edn. Princeton Univ. Press, Princeton, NJ
Blais-Ouellette S., Carignan C., Amram P., Côté S., 1999, AJ, 118, 2123
Blais-Ouellette S., Amram P., Carignan C., 2001, AJ, 121, 1952
Bouché N., Carfantan H., Schroetter I., Michel-Dansac L., Contini T., 2015, AJ, 150, 92
Boulares A., Cox D. P., 1990, ApJ, 365, 544
Bowyer S., Lieu R., Sidher S. D., Lampton M., Knude J., 1995, Nature, 375, 212
Boylan-Kolchin M., Springel V., White S. D. M., Jenkins A., Lemson G., 2009, MNRAS, 398, 1150
Broeils A. H., van Woerden H., 1994, A&AS, 107, 129
Ceverino D., Klypin A., 2009, ApJ, 695, 292
Chabrier G., 2003, PASP, 115, 763
Chan T. K., Kereš D., Oñorbe J., Hopkins P. F., Muratov A. L., Faucher-Giguère C.-A., Quataert E., 2015, MNRAS, 454, 2981
Chemin L., Huré J.-M., Soubiran C., Zibetti S., Charlot S., Kawata D., 2016, A&A, 588, A48
Cinzano P., Rix H.-W., Sarzi M., Corsini E. M., Zeilinger W. W., Bertola F., 1999, MNRAS, 307, 433
Cox T. J., 2004, PhD thesis, Univ. California
Cox D. P., 2005, ARA&A, 43, 337
de Blok W. J. G., Bosma A., 2002, A&A, 385, 816
de Blok W. J. G., McGaugh S. S., 1997, MNRAS, 290, 533
de Blok W. J. G., van der Hulst J. M., Bothun G. D., 1995, MNRAS, 274, 235
de Blok W. J. G., McGaugh S. S., Bosma A., Rubin V. C., 2001, ApJ, 552, L23
de Blok W. J. G., Bosma A., McGaugh S., 2003, MNRAS, 340, 657
de Blok W. J. G., Walter F., Brinks E., Trachternach C., Oh S.-H., Kennicutt R. C., Jr, 2008, AJ, 136, 2648
Dalcanton J. J., Stilp A. M., 2010, ApJ, 721, 547
Davis M., Efstathiou G., Frenk C. S., White S. D. M., 1985, ApJ, 292, 371
Di Teodoro E. M., Fraternali F., 2015, MNRAS, 451, 3021
Diemand J., Zemp M., Moore B., Stadel J., Carollo C. M., 2005, MNRAS, 364, 665
Du W., Wu H., Lam M. I., Zhu Y., Lei F., Zhou Z., 2015, AJ, 149, 199
Dutton A. A., Courteau S., de Jong R., Carignan C., 2005, ApJ, 619, 218
Elmegreen B. G., Scalo J., 2004, ARA&A, 42, 211
Epinat B. et al., 2008a, MNRAS, 388, 500
Epinat B., Amram P., Marcelin M., 2008b, MNRAS, 390, 466
Epinat B., Amram P., Balkowski C., Marcelin M., 2010, MNRAS, 401, 2113
Fathi K., Beckman J. E., Zurita A., Relaño M., Knapen J. H., Daigle O., Hernandez O., Carignan C., 2007, A&A, 466, 905
Ferrière K. M., 2001, Rev. Mod. Phys., 73, 1031
Field G. B., Goldsmith D. W., Habing H. J., 1969, ApJ, 155, L149
Flores R. A., Primack J. R., 1994, ApJ, 427, L1
Garrido O., Marcelin M., Amram P., Boulesteix J., 2002, A&A, 387, 821
Garrison-Kimmel S., Rocha M., Boylan-Kolchin M., Bullock J. S., Lally J., 2013, MNRAS, 433, 3539
Gelato S., Sommer-Larsen J., 1999, MNRAS, 303, 321
Gnedin O. Y., Zhao H., 2002, MNRAS, 333, 299
Governato F. et al., 2010, Nature, 463, 203
Governato F. et al., 2012, MNRAS, 422, 1231
Guo Q., White S., Li C., Boylan-Kolchin M., 2010, MNRAS, 404, 1111
Hayashi E., Navarro J. F., Springel V., 2007, MNRAS, 377, 50
Hayward C. C., Torrey P., Springel V., Hernquist L., Vogelsberger M., 2014, MNRAS, 442, 1992
Hopkins P. F., Kereš D., Oñorbe J., Faucher-Giguère C.-A., Quataert E., Murray N., Bullock J. S., 2014, MNRAS, 445, 581
Hunter D. A. et al., 2012, AJ, 144, 134

Impey C., Bothun G., 1997, ARA&A, 35, 267
Kamphuis P., Józsa G. I. G., Oh S.-H., Spekkens K., Urbancic N., Serra P., Koribalski B. S., Dettmar R.-J., 2015, MNRAS, 452, 3139
Kazantzidis S., Abadi M. G., Navarro J. F., 2010, ApJ, 720, L62
Klypin A., Kravtsov A. V., Bullock J. S., Primack J. R., 2001, ApJ, 554, 903
Klypin A., Yepes G., Gottlober S., Prada F., Hess S., 2016, MNRAS, 457, 4340
Kormendy J., Freeman K. C., 2016, ApJ, 817, 84
Krajnović D., Cappellari M., de Zeeuw P. T., Copin Y., 2006, MNRAS, 366, 787
Kuzio de Naray R., Kaufmann T., 2011, MNRAS, 414, 3617
Kuzio de Naray R., McGaugh S. S., de Blok W. J. G., Bosma A., 2006, ApJS, 165, 461
Kuzio de Naray R., McGaugh S. S., de Blok W. J. G., 2008, ApJ, 676, 920
Kuzio de Naray R., McGaugh S. S., Mihos J. C., 2009, ApJ, 692, 1321
Lia C., Carraro G., Salucci P., 2000, A&A, 360, 76
Ludlow A. D., Navarro J. F., Angulo R. E., Boylan-Kolchin M., Springel V., Frenk C., White S. D. M., 2014, MNRAS, 441, 378
Mac Low M.-M., Klessen R. S., 2004, Rev. Mod. Phys., 76, 125
McKee C. F., Ostriker J. P., 1977, ApJ, 218, 148
Madau P., Shen S., Governato F., 2014, ApJ, 789, L17
Marinacci F., Pakmor R., Springel V., 2014, MNRAS, 437, 1750
Mashchenko S., Wadsley J., Couchman H. M. P., 2008, Science, 319, 174
Moore B., 1994, Nature, 370, 629
Moore B., Quinn T., Governato F., Stadel J., Lake G., 1999, MNRAS, 310, 1147
Navarro J. F., Eke V. R., Frenk C. S., 1996a, MNRAS, 283, L72
Navarro J. F., Frenk C. S., White S. D. M., 1996b, ApJ, 462, 563
Navarro J. F., Frenk C. S., White S. D. M., 1997, ApJ, 490, 493
Navarro J. F. et al., 2004, MNRAS, 349, 1039
Oh S.-H., de Blok W. J. G., Walter F., Brinks E., Kennicutt R. C., Jr, 2008, AJ, 136, 2761
Oh S.-H., de Blok W. J. G., Brinks E., Walter F., Kennicutt R. C., Jr, 2011a, AJ, 141, 193
Oh S.-H., Brook C., Governato F., Brinks E., Mayer L., de Blok W. J. G., Brooks A., Walter F., 2011b, AJ, 142, 24
Oh S.-H. et al., 2015, AJ, 149, 180
Oman K. A. et al., 2015, MNRAS, 452, 3650
Oñorbe J., Boylan-Kolchin M., Bullock J. S., Hopkins P. F., Kereš D., Faucher-Giguère C.-A., Quataert E., Murray N., 2015, MNRAS, 454, 2092
Ott J. et al., 2012, AJ, 144, 123
Persic M., Salucci P., 1995, ApJS, 99, 501
Pontzen A., Governato F., 2014, Nature, 506, 171
Power C., Navarro J. F., Jenkins A., Frenk C. S., White S. D. M., Springel V., Stadel J., Quinn T., 2003, MNRAS, 338, 14
Read J. I., Gilmore G., 2005, MNRAS, 356, 107
Read J. I., Iorio G., Agertz O., Fraternali F., 2016, MNRAS, 462, 3628
Rhee G., Valenzuela O., Klypin A., Holtzman J., Moorthy B., 2004, ApJ, 617, 1059
Roberts M. S., Haynes M. P., 1994, ARA&A, 32, 115

Salpeter E. E., 1955, ApJ, 121, 161
Salucci P., 2001, MNRAS, 320, L1
Sawala T., Scannapieco C., Maio U., White S., 2010, MNRAS, 402, 1599
Sawala T. et al., 2016, MNRAS, 457, 1931
Schaller M. et al., 2015, MNRAS, 451, 1247
Schaye J. et al., 2015, MNRAS, 446, 521
Simon J. D., Bolatto A. D., Leroy A., Blitz L., 2003, ApJ, 596, 957
Simon J. D., Bolatto A. D., Leroy A., Blitz L., Gates E. L., 2005, ApJ, 621, 757
Spano M., Marcelin M., Amram P., Carignan C., Epinat B., Hernandez O., 2008, MNRAS, 383, 297
Sparre M., Hayward C. C., Feldmann R., Faucher-Giguère C.-A., Muratov A. L., Kereš D., Hopkins P. F., 2015, preprint (arXiv:1510.03869)
Spekkens K., Giovanelli R., Haynes M. P., 2005, AJ, 129, 2119
Springel V., 2005, MNRAS, 364, 1105
Springel V., 2010, MNRAS, 401, 791
Springel V., Hernquist L., 2003, MNRAS, 339, 289
Springel V. et al., 2005, Nature, 435, 629
Stadel J., Potter D., Moore B., Diemand J., Madau P., Zemp M., Kuhlen M., Quilis V., 2009, MNRAS, 398, L21
Stark D. V., McGaugh S. S., Swaters R. A., 2009, AJ, 138, 392
Su K.-Y., Hopkins P. F., Hayward C. C., Faucher-Giguere C.-A., Keres D., Ma X., Robles V. H., 2016, preprint (arXiv:1607.05274)
Swaters R. A., Madore B. F., Trewhella M., 2000, ApJ, 531, L107
Swaters R. A., Madore B. F., van den Bosch F. C., Balcells M., 2003, ApJ, 583, 732
Trachternach C., de Blok W. J. G., Walter F., Brinks E., Kennicutt R. C., Jr, 2008, AJ, 136, 2720
van Albada T. S., Bahcall J. N., Begeman K., Sancisi R., 1985, ApJ, 295, 305
van den Bosch F. C., Swaters R. A., 2001, MNRAS, 325, 1017
van den Bosch F. C., Robertson B. E., Dalcanton J. J., de Blok W. J. G., 2000, AJ, 119, 1579
Valenzuela O., Rhee G., Klypin A., Governato F., Stinson G., Quinn T., Wadsley J., 2007, ApJ, 657, 773
Verdoes Kleijn G. A., van der Marel R. P., Carollo C. M., de Zeeuw P. T., 2000, AJ, 120, 1221
Vogelsberger M. et al., 2014a, MNRAS, 444, 1518
Vogelsberger M., Zavala J., Simpson C., Jenkins A., 2014b, MNRAS, 444, 3684
Vogelsberger M. et al., 2014c, Nature, 509, 177
Walker M. G., Peñarrubia J., 2011, ApJ, 742, 20
Walter F., Brinks E., de Blok W. J. G., Bigiel F., Kennicutt R. C., Jr, Thornley M. D., Leroy A., 2008, AJ, 136, 2563
Weijmans A.-M., Krajnović D., van de Ven G., Oosterloo T. A., Morganti R., de Zeeuw P. T., 2008, MNRAS, 383, 1343

This paper has been typeset from a TEX/LATEX file prepared by the author.